Clinical Intravoxel Incoherent Motion and Diffusion MR Imaging: Past, Present, and Future[1]

Mami Iima, MD, PhD
Denis Le Bihan, MD, PhD

The concept of diffusion magnetic resonance (MR) imaging emerged in the mid-1980s, together with the first images of water diffusion in the human brain, as a way to probe tissue structure at a microscopic scale, although the images were acquired at a millimetric scale. Since then, diffusion MR imaging has become a pillar of modern clinical imaging. Diffusion MR imaging has mainly been used to investigate neurologic disorders. A dramatic application of diffusion MR imaging has been acute brain ischemia, providing patients with the opportunity to receive suitable treatment at a stage when brain tissue might still be salvageable, thus avoiding terrible handicaps. On the other hand, it was found that water diffusion is anisotropic in white matter, because axon membranes limit molecular movement perpendicularly to the nerve fibers. This feature can be exploited to produce stunning maps of the orientation in space of the white matter tracts and brain connections in just a few minutes. Diffusion MR imaging is now also rapidly expanding in oncology, for the detection of malignant lesions and metastases, as well as monitoring. Water diffusion is usually largely decreased in malignant tissues, and body diffusion MR imaging, which does not require any tracer injection, is rapidly becoming a modality of choice to detect, characterize, or even stage malignant lesions, especially for breast or prostate cancer. After a brief summary of the key methodological concepts beyond diffusion MR imaging, this article will give a review of the clinical literature, mainly focusing on current outstanding issues, followed by some innovative proposals for future improvements.

Online supplemental material is available for this article.

[1] From the Department of Diagnostic Imaging and Nuclear Medicine (M.I.) and the Human Brain Research Center (D.L.B.), Kyoto University Graduate School of Medicine, and the Hakubi Center for Advanced Research (M.I.), Kyoto University, Kyoto, Japan; and NeuroSpin, CEA/DSV/I^{2}BM, Bât 145, Point Courrier 156, CEA-Saclay Center, F-91191 Gif-sur-Yvette, France (D.L.B.). Received February 5, 2015; revision requested April 14; final revision received May 29; accepted June 30; final version accepted July 21. **Address correspondence to** D.L.B. (e-mail: *denis.lebihan@cea.fr*).

In 1905 Albert Einstein published four important articles and set the stage for all of modern physics. One of his annus mirabilis articles (also his PhD thesis dissertation) unexpectedly gave birth to a powerful medical imaging modality, diffusion magnetic resonance (MR) imaging (1). The concept of diffusion MR imaging emerged in the mid-1980s, together with the first images of water molecular diffusion in the human brain (2), as a way to probe tissue structure at a microscopic scale, although images were acquired at a millimetric scale (3). Since then, diffusion MR imaging has become a pillar of modern clinical imaging. Diffusion MR imaging is both a method and a powerful concept, as diffusing water molecules provide unique information on the tissue functional architecture. Diffusion MR imaging has mainly been used to investigate neurologic disorders. A dramatic application of diffusion MR imaging has been acute brain ischemia, following the discovery that water diffusion drops immediately after the onset of an ischemic event, when brain cells undergo swelling through cytotoxic edema. With its unmatched sensitivity, water diffusion MR imaging provides patients with the opportunity to receive suitable treatment at a stage when brain tissue might be still salvageable, thus avoiding them permanent loss of function. On the other hand, it was found that water diffusion is anisotropic in white matter, because axon membranes limit molecular movement perpendicularly to the nerve fibers. This feature can be exploited to produce stunning maps of the orientation in space of the white matter tracts and brain connections in just a few minutes, as well as to provide information on white matter microstructure and integrity. With water diffusion MR imaging it has been suggested that some psychiatric disorders, such as schizophrenia, might result from faulty brain connections. Further work has shown (4) that diffusion MR imaging can work well in the body with free breathing and background signal suppression. Use of the technique is now also rapidly expanding in oncology for the detection of malignant lesions and metastases, as well as monitoring therapy. Water diffusion is substantially decreased in malignant tissues, and body diffusion MR imaging, which does not require any tracer injection, is rapidly becoming modality of choice to detect, characterize, or even stage malignant lesions, especially breast and prostate cancer. Since its introduction, diffusion MR imaging has enjoyed a quasi-exponential growth, with about 24 000 articles referenced in PubMed in 2014 and 725 000 entries in Google Scholar (Fig 1). However, as MR imaging scanner gradient coil systems, a key hardware component for diffusion MR imaging, have been greatly improved over the recent years, new trends have emerged beyond the original apparent diffusion coefficient (ADC) concept: IVIM is entering the clinical field to evaluate tissue perfusion without use of contrast agents, and the ability to analyze non-Gaussian diffusion through high diffusion weighting is boosting sensitivity to tissue features.

After a brief summary of the key concepts beyond diffusion MR imaging, we will give a review of key areas of clinical application. This review is of necessity not comprehensive, given the huge amount of literature on the subject. Rather, it will focus on current outstanding issues, followed by some proposals for future improvements.

Essentials

- Diffusion MR imaging has become a pillar of modern clinical imaging, mainly to investigate the diseased brain, but is also increasingly been used in the body, notably in oncology.
- Important issues must be considered when interpreting diffusion MR imaging results: diffusion anisotropy, non-Gaussian diffusion, intravoxel incoherent motion, and noise effects.
- Some issues still need to be addressed for diffusion MR imaging to become a clinical biomarker, especially standardization of acquisition protocols and models used for quantitative image analysis.
- In the future, methods may allow tissue features to be obtained directly from a limited set of diffusion MR imaging signals based on their signature, substantially reducing acquisition and processing times.

Key Concepts to Understand and Interpret Diffusion and IVIM MR Imaging

Diffusion and Brownian Motion

Brownian motion refers to the spontaneous random motion of particles suspended in a fluid. This phenomenon is named after the botanist Robert Brown, who in 1827 observed through a microscope that pollen grains moved through the water. Independently, the phenomenon of diffusion, referring to the net movement of a substance from a region of high concentration to a region of low concentration, had been fully characterized by the Fick laws. Einstein explained later in his PhD thesis and its companion article (1) how Brownian motion was explained by the particles being moved by individual molecules, and how their displacement was linked to the diffusion coefficient (D) of the Fick laws, bridging for the first time the macroscopic diffusion and microscopic Brownian motion concepts. This explanation of Brownian motion served as definitive confirmation that atoms and molecules actually exist and was further verified experimentally in 1908 by Jean Perrin, who used it to determine the

Published online
10.1148/radiol.2015150244 **Content code:** MR

Radiology 2016; 278:13–32

Abbreviations:
ADC = apparent diffusion coefficient
D = diffusion coefficient
D^* = pseudodiffusion coefficient
DTI = diffusion-tensor imaging
FDG = fluorodeoxyglucose
fIVIM = flowing blood volume fraction
IVIM = intravoxel incoherent motion

Conflicts of interest are listed at the end of this article.

Figure 1

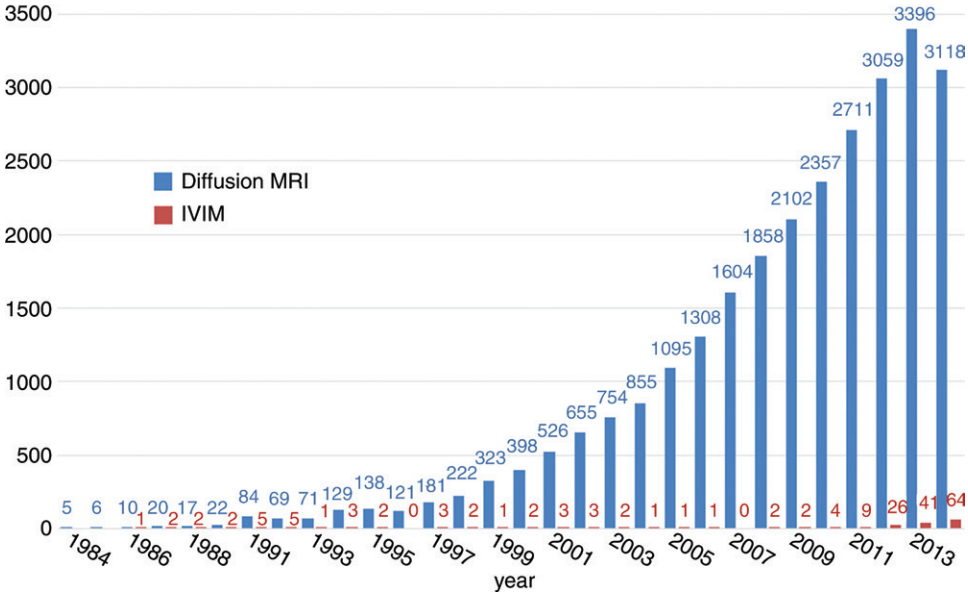

Figure 1: Graph shows the number of articles (vertical axis) published on diffusion and intravoxel incoherent motion (IVIM) MR imaging since 1984, including both clinical and preclinical studies.

Avogadro number and the size of the water molecule (5).

With diffusion MR imaging one usually investigates the self-diffusion of water molecules in tissue water (diffusion of other molecular moities may also be studied with MR spectroscopy). Diffusion-driven displacements of water molecules are encoded in the MR imaging signal through variations of the magnetic field in space (6,7) caused by magnetic field gradient pulses. The degree of sensitivity to diffusion is described by the so-called *b* value, which was introduced (2,8) to take into account the intensity and time profile of the gradient pulses used both for diffusion encoding and MR imaging spatial encoding. The overall effect of diffusion in the presence of those gradient pulses is signal attenuation, and the MR imaging signal becomes diffusion weighted. The signal attenuation is more pronounced when large *b* values are used and when diffusion is fast.

Diffusion Anisotropy

A first important consequence of the diffusion MR imaging encoding process (compared with other approaches) is that diffusion, although a three-dimensional process, is only measured along one direction at a time determined by the orientation in space of the gradient pulses. Most often diffusion is isotropic (the same in all directions), so that this spatial orientation does not matter. In some tissues, however, such as brain white matter or muscle fibers, diffusion is anisotropic, and diffusion effects strongly depend on the direction of the gradient pulse. It is often thought by those in clinical practice and by MR imaging manufacturers that one gets a "mean" diffusivity effect by averaging images sequentially acquired with gradients oriented along three perpendicular directions. It can easily be shown that this is only an approximation (7), which may lead to a large overestimation of the true mean ADC in tissues experiencing anisotropic diffusion, especially when diffusion pulses are set on several axes at the same time (to minimize echo time and increase signal-to-noise ratio). For instance, even if the diffusion-encoding gradient pulses are set only to the x-axis, any gradient pulse present on the y- or z-axis will combine with the diffusion-encoding pulses on the x-axis and also contribute to the diffusion signal if diffusion-coupling terms (*D*xy, *D*xz) exist, which is the case when the tissue feature axes do not coincide with the gradient directions used for measurements. This mean ADC is then not rotationally invariant. Anisotropic diffusion cannot be correctly described by three diffusion coefficients along three directions, but requires the acquisition of diffusion-weighted images along at least six different directions (diffusion-tensor imaging [DTI] [9]). With DTI, one can get the trace of the diffusion tensor, which represents the true mean diffusivity, indexes of the degree of anisotropy (such as fractional anisotropy), and so-called eigenvectors, which point to the directions along which diffusion is the fastest or the lowest, corresponding in general to the directions parallel or perpendicular to the tissue fibers, respectively (7). DTI has served as the basis for brain white matter tractography, but more advanced techniques are currently used to take into account voxels with multiple fiber orientations (6). DTI must be used in tissues where water diffusion is anisotropic, mainly in the heart, muscle, and brain white

matter, but other tissues may unexpectedly also show signs of anisotropy, such as the breast or the kidney, due to the presence of spatially oriented ducts (10,11).

The ADC Concept

Another important point is that the Einstein equation, which has been used as a basis for diffusion MR imaging, assumes free diffusion, as can be found in a glass of water. With free diffusion, the distribution of diffusion-driven molecular displacements obeys Gaussian law. In those conditions only the diffusion coefficient, which can be obtained by processing diffusion-weighted images, is the true diffusion coefficient. This coefficient, which depends on temperature (2.4% change per 1°C), is around 3.0 $\times$ 10^{-3} mm^2/sec at 37°C. In biologic tissues, however, diffusion is no longer free, but becomes hindered by obstacles such as cell membranes, fibers, or macromolecules or is confined by attractive centers such as electric charges at the proteins or cell membrane surfaces, making diffusion MR imaging exquisitely sensitive to tissue structure in various pathologic or physiologic conditions. The molecular displacement distribution then deviates from a Gaussian law and the diffusion effect on the MR imaging signal is no longer adequately described by the Einstein equation. Consequently, the diffusion coefficient derived from diffusion-weighted images is no longer the true diffusion coefficient, but reflects interaction of water with tissue features. The modeling of such diffusion effects on the signal had been investigated by pioneers such as Stejskal, Tanner, Hazlewood, and others (12) well before the advent of MR imaging, but this issue remains a complex and hot topic of investigation today (13). The ADC concept was introduced along with the diffusion MR imaging concept to avoid those difficulties in a clinical setting (2). The idea was to still use the Einstein equation to simply model diffusion MR imaging signals (as if water diffusion was Gaussian), but to describe the results as an ADC to emphasize that results would differ from the true diffusion coefficient if that were measureable. This concept has proved extremely powerful and durable, and the ADC is still widely used today (14).

The IVIM Concept

The ADC concept was also introduced to encompass all types of incoherent motion present within each image voxel (hence, the acronym IVIM), which could contribute to the signal attenuation observed with diffusion MR imaging, such as blood microcirculation in the capillary networks (perfusion), and not only molecular diffusion (15). Indeed, flow of blood water in randomly oriented capillaries (at voxel level) mimics a random walk (pseudodiffusion), which results in a signal attenuation in the presence of the diffusion-encoding gradient pulses. The effect is seen at very low *b* values only, because the pseudodiffusion coefficient, *D**, associated with blood flow is higher than the water diffusion coefficient. For this reason, the ADC obtained by including very-low-*b*-value signals is usually higher than when larger values are used (14). On the other hand, the one order of magnitude or so difference between true diffusion and pseudodiffusion allows them to be separated (15,16). The idea to use diffusion and IVIM MR imaging to get images of perfusion has been found ground-breaking (17), however very controversial at the beginning, and it took more than 20 years before the concept was applied in clinical practice. Indeed, IVIM MR imaging has experienced a remarkable revival for applications throughout the body over the last few years (3) (Fig 1), especially in the field of cancer imaging. A key feature of IVIM diffusion MR imaging is that it does not involve contrast agents, and it may serve as an interesting alternative to perfusion MR imaging in some patients with contraindications to contrast agents or patients with renal failure at risk for nephrogenic systemic fibrosis (18,19) or for gadolinium deposits in brain basal ganglia (20). Still, a deeper insight into the IVIM concept and a clear understanding of the strengths and limitations of the concept are necessary to fully garner the benefit of the method in the clinical setting. Specifically, the relationship of IVIM parameters (*D** and flowing blood volume fraction [fIVIM]) with blood volume and blood flow estimates using other approaches needs to be clarified. Separation of perfusion from diffusion requires high signal-to-noise ratios, and there are some technical challenges to overcome, such artifacts from other bulk flow phenomena. Vascular and tubular flow may be difficult to disentangle in some tissues, such as the kidney (21). Active transport resulting from glandular secretion (breast ducts, salivary glands and pancreas) may also be difficult to separate from microcapillary perfusion. One also has to keep in mind that IVIM imaging has a differential sensitivity to vessel sizes, according to the range of *b* values that are used.

The *b*-Value Effect

Another important feature is that diffusion compared with other parameters, such as T1 or T2, is a genuine physical process occurring in tissues on its own, not linked to MR imaging (MR imaging is merely a means to investigate it), as opposed to T1 or T2, which are only defined in the MR imaging context and depend heavily, for instance, on the field strength and MR imaging sequences. In contrast, the results of diffusion MR imaging, such as the ADC, should be, in principle, equivalent across centers using different MR imaging systems or sequence parameters. Unfortunately, this is true only to some extent: Problems may arise, as noted above, because diffusion in tissues in not free. With free (Gaussian) diffusion, the ADC remains the same whichever set of *b* values are used to measure it (only the accuracy of the ADC estimates will change with the *b* values, and it is well known that the optimal *b* value for brain tissue, for instance, is around 1000 sec/mm^2). When diffusion is non-Gaussian, the degree of diffusion-related signal attenuation decreases when the *b* value increases (Fig 2), in other words, the ADC value decreases when high *b* values are used. It is, thus, mandatory to indicate which *b* values have been used to acquire

Figure 2

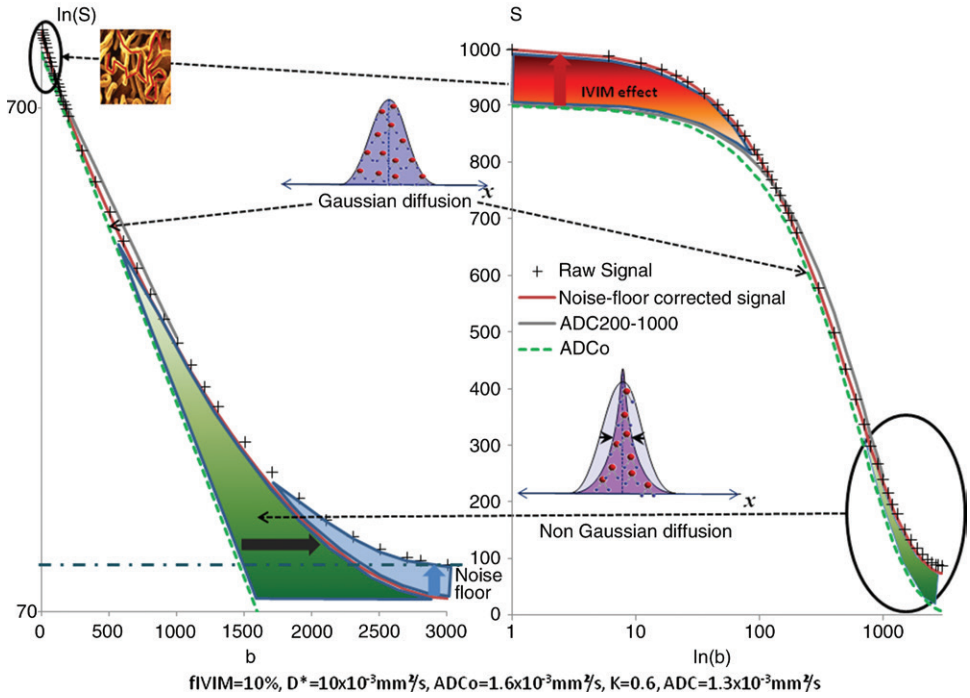

Figure 2: Diffusion MR imaging signal attenuation. Left: The natural logarithm of the signal attenuation shows a triple curvature. At low *b* values (< 200 sec/mm^2), the curvature results from IVIM (blood microcirculation) effects (here the *f*IVIM has been set to 10%). At very high *b* values, the signal reaches a "noise floor," which produces a curvature that needs to be removed before signal analysis. The curvature visible at high *b* values after noise correction (deviation from the straight line expected for free diffusion) is produced by hindrance effects (notably from membranes), which make diffusion non-Gaussian. The kurtosis model is one approach that allows this non-Gaussian diffusion effect to be quantified. At lower *b* values the signal attenuation is nearly straight, as with Gaussian diffusion. The slope obtained by using two *b* values (such as 200 and 1000 sec/mm^2) is smaller than the Gaussian diffusion component of the signal ADC_0, which is obtained by removing the non-Gaussian component, for instance, using the kurtosis model (Eq [1]). Right: Since the IVIM effect is usually small, more images are often acquired at low *b* values than for diffusion at high *b* values. However, it may be difficult to visually qualify the goodness of the diffusion and IVIM fits using the standard attenuation plot: ln(S) as a function of *b* value, as in the left plot, where *S* is signal intensity. An attractive alternative would be to plot *S* as a function of ln(b) to visually exaggerate the contribution of IVIM effects at very low *b* values.

data if one wishes to make meaningful comparisons across literature. In fact, not only the *b* values, but the precise timing of the gradient pulses (which set the diffusion time) used for diffusion encoding must be provided, as different time profiles could lead to different diffusion effects while sharing the same *b* value. This is due to the fact that water molecules will have more chances to interact with tissue microscopic features when long diffusion times are used than when short diffusion times are used, leading to lesser signal attenuation and, thus, to a smaller ADC at long diffusion times (22).

Non-Gaussian Diffusion Models

Such non-Gaussian diffusion effects become visible, however, only when high *b* values are used, which is now possible thanks to the progress made in gradient hardware. While achievable *b* values in the mid-1980s were in the range of 100 sec/mm^2, they extended to around 1000 sec/mm^2 in the 1990s, to easily reach 3000 sec/mm^2 today, or even above 20 000 sec/mm^2 in some prototype gradient systems made available for the Human Connectome Project (23) or in preclinical systems where gradient amplitudes of 1000 mT/m are not uncommon (compared with 30–80 mT/m in clinical systems). By using such high *b* values, the ADC concept (also often referred to as the monoexponential model) reaches its limitation, as it cannot give a proper account of the curvature of the signal attenuation (in semilog coordinates) that becomes apparent at high *b* values (Fig 2). Indeed, some extremely valuable information on tissue structure can be found in this curvature (14), and several models have been suggested to empirically handle this non-Gaussian behavior, such as the polynomial or kurtosis model (24) (also called diffusion kurtosis imaging [25]), the biexponential

model (26), the statistical model (27), the stretched exponential model (28), and others (29,30). With such models new parameters have emerged beyond the ADC, such as the kurtosis for diffusion kurtosis imaging, which have shown great potential to characterize pathologic or physiologic conditions, although they only give empirical information on the degree of diffusion non-Gaussianity and nothing specific on tissue features. These models have been used to evaluate cerebral infarction (31), liver fibrosis (32), and tumor characterization (33,34). Other models have been designed not just to mathematically describe the signal decay with *b* values, but to provide more insightful, explanatory information on the tissue features, mainly in the brain, such as the axon diameter in white matter (composite hindered and restricted model of diffusion, or CHARMED (35), and AxCaliber models [36]) or for the gray matter neurite distribution (neurite orientation dispersion and density imaging, or NODDI, model [37]). However, those extremely refined models require strong assumptions on the underlying tissue structure, sophisticated modeling and analysis, and still must be validated across the full range of clinical conditions. It is understandable that clinicians might be puzzled by this array of diffusion models and the variety of ways to process the diffusion-weighted images they require. However, clinically relevant images can be derived from parametric maps produced by combining images acquired with a range of *b* values according to the relevant physical models by using one's preferred software, either in-house or provided by vendors. Such maps often allow one, in particular, to assess lesion heterogeneity.

Data Analysis and Noise Effects

A last important issue to consider is the effect of noise on the output produced by such models if one wants to get meaningful information. There is still another cause of curvature of the signal attenuation than non-Gaussian diffusion at high *b* values: noise. At high *b* values, because of the nature of the MR imaging signal (a magnitude signal that cannot be negative), there is always some background noise signal left and the diffusion signal remains above a threshold, the noise floor (Fig 2), instead of asymptotically approaching 0, thus mimicking a curvature effect (16). Such noise effects must be corrected, if present, to avoid over- or underestimation of the model outputs (ADC, kurtosis, fIVIM, etc), which is not a trivial matter. Several approaches have been proposed to correct this noise at high *b* values, either by retrieving signal values from noise-corrupted data (38–42) or by using a simple procedure where a noise-correction factor is estimated through a phantom calibration process (16). As a matter of fact, alcanes should be preferred to build phantoms, as they offer a wide range of ADC values mimicking biologic tissues or diseases and are less prone to artifacts than water or ice (43) (fat suppression must be turned off during measurements, though, as the alcanes resonant frequency is close to that of fat). Those noise effects may explain discrepancies among the various diffusion MR imaging and IVIM parameter values in the literature.

Another issue related to noise is that model parameter estimates may depend on the algorithms that are used to fit the signals with the model equations. One may fit the model equation at once (including IVIM, non-Gaussian diffusion, and noise effects together), for instance, by using an "Exhaustive" search algorithm [16]), while a popular way is to split the fitting into two steps, one for diffusion and the other for IVIM effects, to increase the robustness of iterative fitting algorithms. This is often referred to as the biexponential approach (one for IVIM and one for diffusion), but should not be confused with the non-Gaussian biexponential diffusion model (26). In fact, taking IVIM and non-Gaussian diffusion altogether one should rather think of triexponential or exponential-polynomial models. An outstanding issue is then to decide the threshold for the *b* value above which IVIM effects can be considered as negligible. This value is often thought to be around 200–400 sec/mm^2, but may extend to 600 sec/mm^2 in the brain and is expected to vary across organs and pathologic conditions. In addition, images with *b* of 0 sec/mm^2 cannot be acquired, as gradient pulses used for imaging are responsible for some (tiny) IVIM and diffusion effects (lowest *b* value achievable is often around 5–10 sec/mm^2 or even sometimes 50 sec/mm^2). Hence, a very good estimation of the theoretical signal at *b* of 0 sec/mm^2 is required to get a meaningful estimate of fIVIM. Furthermore, while the IVIM effects reflecting microcirculation are seen only at very low *b* values, they are usually very small and require a very good handling of the whole signal curvature, even at very large *b* values (including non-Gaussian diffusion and noise floor correction) to give correct estimates of parameters (16).

With those concepts in mind, we will now briefly review the clinical field of applications of diffusion and IVIM MR imaging.

Review of Clinical Applications

Neuroimaging

Acute and chronic stroke.—There is no doubt that the main application of diffusion MR imaging has been for the diagnosis of acute cerebral infarction (44), as well as the estimation of the time course of ADC change in stroke (45). The ADC decrease occurring minutes after the ischemic insult is linked to cell swelling through cytotoxic edema, but the basic mechanisms remain unclear (12,46,47). Diffusion MR imaging has resulted in substantial changes to the treatment of patients with stroke, allowing physicians to customize therapeutic approaches (pharmacological or interventional) for individual patients (48), as well as monitoring patient progress on an objective basis (in both the acute and the chronic phase [49]), to help predict clinical outcome (48,50–52). At high degree of diffusion weighing, as seen through the mean kurtosis, sensitivity to tissue features increases, improving the characterization of ischemic tissues (53). IVIM MR imaging

also has potential for the management of cerebral infarction (54) or to assess the brain's microvasculature pulsatility on the cardiac cycle (55).

White matter diseases and tractography.—DTI has mainly been used in neuroscience (6); however, it is gaining momentum as a clinical tool. DTI can help estimate the relationship between tumors and nearby white matter tracts for preoperative and intraoperative planning (56). DTI is commonly used to investigate white matter disorders and has also revealed faulty brain connections linked to psychiatric disorders, such as schizophrenia, bipolar disorder, and anxiety disorder (57). Diffusion-weighted imaging and DTI have been increasingly applied to the clinical investigation of demyelinating disease, especially multiple sclerosis, and correlations have been shown between diffusion-weighted imaging findings and clinical symptoms of multiple sclerosis (58). In addition, an ADC decrease in acute disseminated encephalomyelitis has been observed, which becomes more prominent during the subacute phase (59). The ADC decrease in the hyperacute phase of a demyelinating lesion might appear even ahead of contrast enhancement (60). Interestingly, tract-based spatial statistics analysis of DTI data appears robust than region-of-interest–based analysis to predict motor outcome in primary progressive multiple sclerosis (61) and detect widespread white matter lesions with a significant fractional anisotropy decrease in patients with neuromyelitis optica, which is useful for the better understanding of the disease (62). DTI also has been shown to be useful to assess brain lesions after mild traumatic brain injury, which is associated with cognitive and physical symptoms, although there are no remarkable findings on conventional MR or computed tomographic (CT) images (63). A recent study has revealed that fractional anisotropy values in the cerebellum and fusiform gyri were lower in patients with mild traumatic brain injury and vestibular symptoms, suggesting DTI as a diagnostic tool for the evaluation of concussion (64). Nonetheless, DTI and resting-state functional connectivity MR imaging have shown some discrepancies in their results, and further investigation is needed to establish the relationship between structural and functional lesions associated with concussion (65).

Oncology

Diffusion MR imaging has great potential as a tool in the treatment of cancer patients, allowing earlier detection, diagnosis, staging, and monitoring of disease progression or response to therapy (66). This approach is complementary to fluorodeoxyglucose (FDG) positron emission tomography (PET), which seems to be more sensitive in lungs and perhaps in lymph nodes (67), but diffusion MR imaging, which does not use ionizing radiation and any tracer and affords a better spatial resolution, appears promising for the management of breast, prostate, liver, and thyroid cancers, as well as lymphomas (68). Furthermore, diffusion MR imaging gives access to tissues obscured by sites of physiologic FDG accumulation, such as in the pelvis around the bladder. Differences in findings are expected with FDG PET and diffusion MR imaging as both approaches are based on completely different biophysical mechanisms. FDG PET shows areas with increased glucose metabolism, which can also be present in inflammation (Fig 3). ADC values correlate with tumor cellularity both in humans (69–71) and animals (72,73), and a very low pretreatment ADC is usually associated with aggressive malignancy (74,75), while relatively high pretreatment ADC values might predict a poor response to therapy (76–78). Some studies have shown a correlation between ADC values and tumor grade in humans (79,80) and animals (73). However, cell density is not the only histologic indicator that sets tumor grade, and other histologic features, such as nuclear atypia, may account for the imperfect correlation. Necrotic or cystic tumor components, which show high ADC, could also reduce the association between ADC and cell density. Whole-body diffusion kurtosis imaging has the potential to extract more microstructural information than the ADC (34), as a high-degree diffusion weighting (high *b* values) increases the effect on the signal of obstacles to free diffusion present in tissues, notably cell membranes. IVIM (fIVIM) appears correlated with vessel density (72,81), and recent studies have shown a correlation between flowing blood volume fraction and cerebral blood volume derived from dynamic susceptibility contrast-enhanced MR imaging in gliomas (82,83) or dynamic contrast-enhanced–derived parameters in renal tumors (84), head and neck tumors (85), or breast tumors (86). In light of these promising results, diffusion MR imaging has been investigated as a potential clinical biomarker for the assessment of new drug development, as well as for monitoring drug response in clinical practice (68). To achieve this goal, several issues remain to be addressed (87) notably about the standardization of the acquisition protocols (in particular fat suppression, as the very low diffusion coefficient of fat may mimic low ADC lesions [4]) and the models used for data processing. Investigations on the relationship between the IVIM and diffusion parameters and the underlying tissue structure at microscopic level, as well as changes induced by therapy, must be pursued. Reliability and reproducibility of diffusion MR imaging results must also be assessed to facilitate monitoring disease progression or response to therapy in individual patients.

Brain tumors.—The ADC has been found useful for the differentiation of brain tumors (88), as well as tumor grading (89), and DTI has mainly been used to characterize tumor infiltration or displacement to the white matter around the brain tumor (90). The potential of the ADC to serve as a surrogate marker for treatment response efficacy has emerged (91,92), and, in combination with IVIM, to differentiate high- from low-grade glioma (93). Moreover, regardless of tumor grade, lower ADC values correlated with poor prognosis in malignant astrocytomas (94). Histogram analysis of IVIM parameters may help in differentiating

Figure 3

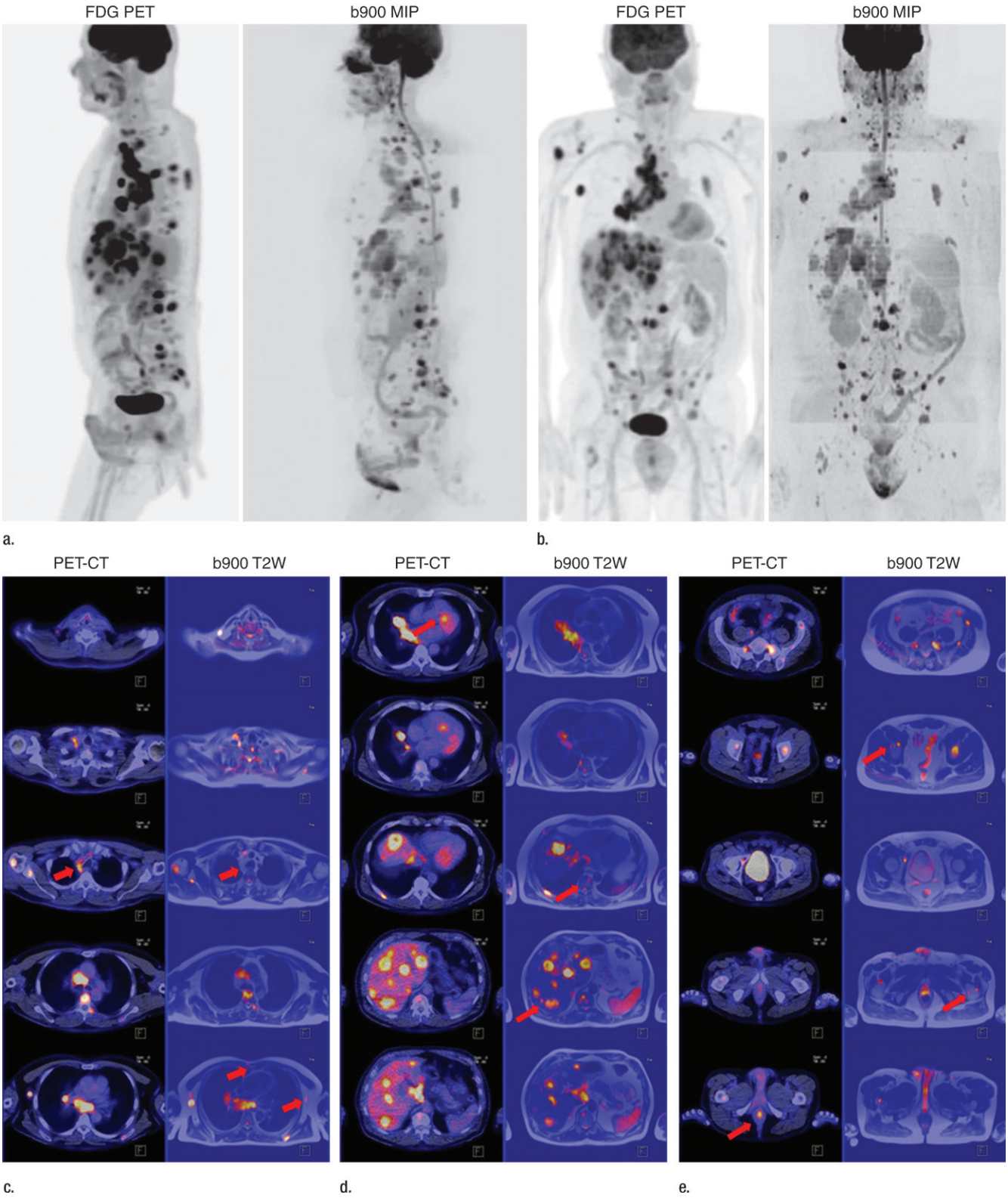
FDG PET
b900 MIP
FDG PET
b900 MIP
a.
b.
PET-CT
b900 T2W
PET-CT
b900 T2W
PET-CT
b900 T2W
c.
d.
e.

recurrent tumor from treatment effect in glioblastoma (83). Diffusion-weighted imaging and DTI have the potential to help determine the optimal radiation treatment volumes (95).

Head and neck.—The evaluation of the head and neck region with MR imaging is hampered by susceptibility artifacts, because of the contiguity of the soft-tissue components with air-filled structures and bone. In addition, some specific movements (eg, jaw movements, swallowing, speaking, coughing, or breathing), as well as respiration, often result in severe motion artifacts. Some methods have been proposed to decrease motion artifacts (96) and to overcome distortion artifacts, such as read-out segmented echo-planar imaging (97). Many studies have confirmed a significant difference in ADC between benign and malignant lesions in this region, but ADC values often overlap between benign and malignant lesions. Parameters derived from non-Gaussian diffusion MR imaging and IVIM might mitigate this limitation for the primary and nonmetastatic head and neck tumors (33). Diffusion and IVIM MR imaging have been applied to salivary gland lesions for the differentiation of benign and malignant tumor, as well as squamous cell carcinomas and lymphomas (98–100). The combination of IVIM and diffusion parameters, each with own threshold for malignancy, results in a better diagnostic ability (98).

The detection of lymph nodal metastases, an important factor for treatment planning, (ie, defining the radiation field or the surgical neck dissection), remains challenging. ADC in malignant nodes seems substantially lower than in benign nodes (101). Primary head and neck tumors have been reported to have a higher IVIM perfusion fraction and ADC compared with metastatic lymph nodes, which could be useful in the optimization of individualized treatment planning (102). Indeed, as nonsurgical therapeutic approaches (radiation therapy and/or chemotherapy) are increasingly used in clinical practice for head and neck cancer, it becomes imperative to identify patients who fail to respond to therapy as early as possible after treatment has been started, so one can change or adjust the treatment regimen if necessary. Although the ADC has been found to increase over the time-course of chemotherapy, especially in squamous cell carcinoma (103,104), its potential to serve as a biomarker of treatment efficacy at an early stage remains controversial and still needs validation. The differentiation of posttherapeutic changes from tumor recurrence is also an important clinical issue, and a recent study using the IVIM model has identified both IVIM and ADC thresholds below which tumor recurrence was likely (105).

Pancreas.—Improvement in gradient hardware and radiofrequency coil systems allowing a good signal-to-noise ratio to be preserved within the images while using high *b* values has made diffusion MR imaging available for the detection and characterization of deep abdominal organs, such as the pancreas. However, there are still some challenges in using ADC values to differentiate pancreatic cancer from mass-forming pancreatitis, due to the variable proportions of fibrosis and inflammation in mass-forming pancreatitis, fibrosis, necrosis, and cell density in tumors (106). IVIM MR imaging seems especially promising as it allows one to differentiate normal pancreatic parenchyma, pancreatic neoplasm (107,108), and mass-foaming pancreatitis (109) with higher diagnostic accuracy than do diffusion-weighted imaging and ADC alone. IVIM MR imaging may also help identify pancreatic adenocarcinoma from other pancreatic masses (neuroendocrine tumor and chronic pancreatitis) (110) and differentiate pancreatic adenocarcinomas from neuroendocrine tumors or benign intraductal papillary mucinous neoplasm (111).

Prostate.—There has been growing interest in multiparametric MR imaging including diffusion MR imaging in the detection, staging, and treatment of prostate cancer (112). Non-Gaussian diffusion has already been investigated in the prostate with the kurtosis (113,114), biexponential (115), or Gamma distribution (116) models. Kurtosis has a better diagnostic ability than simple ADC in differentiating healthy and cancerous peripheral prostate tissues (114) or low- and high-grade prostate cancer (113) (Fig 4). Results have been mixed regarding the diagnostic utility of IVIM in the diagnosis of prostate cancer (117,118), although perfusion-free diffusion coefficient might have a better diagnostic ability than ADC (119). In fact, IVIM perfusion fractions in cancer and normal tissue, as well as their differences, are highly variable within the literature (114,117,118,120–124) (Table E1 [online]), and the application of IVIM in the diagnosis of prostate cancer still needs further validation. Diffusion MR imaging has also great potential in the active surveillance of low-risk patients,

Figure 3: Comparison of diffusion-weighted (*b* value = 900 sec/mm^2 *[b900]*) whole-body imaging with background body signal suppression (DWIBS) and FDG PET in a 62-year-old man with small cell lung cancer showing neuroendocrine differentiation. **(a)** Lateral and **(b)** frontal maximum intensity projection (*MIP*) images of DWIBS and FDG PET (inverted MIP) performed on consecutive days. Grossly there is good concordance of high uptake on FDG PET scan with high-signal-intensity (b = 900 sec/mm^2) MIP images but there are differences on **(c–e)** fused PET/CT (left column) and fused DWIBS and T2-weighted (right column) images. **(c)** Images in the upper chest. The FDG-avid right paratracheal lymph node is not seen as a high-signal-intensity lesion on fused DWIBS/T2-weighted image (third row, arrow). Also, normal left axillary and right internal mammary nodes (fifth row, arrows) visible on fused DWIBS/T2-weighted images are not FDG avid; these lymph nodes are likely to be normal. **(d)** Images in the lower chest and liver. Normal FDG uptake in the heart not seen on fused DWIBS/T2-weighted images (third row, arrow). Liver metastases are more clearly outlined on fused DWIBS/T2-weighted images (fourth row, arrow). Bone deposits are also more clearly seen on fused DWIBS/T2-weighted images (third row, arrow). **(e)** Images in the pelvis. Note increased FDG uptake in the lower anal canal is not seen on fused DWIBS/T2-weighted images (fifth row, arrow); this is presumed to be inflammatory. Bone deposits are more clearly seen on fused DWIBS/T2-weighted images (second and fourth rows, arrows). (Image courtesy of Prof Anwar R. Padhani, Paul Strickland Scanner Centre, Mount Vernon Cancer Centre, London, England.)

Figure 4

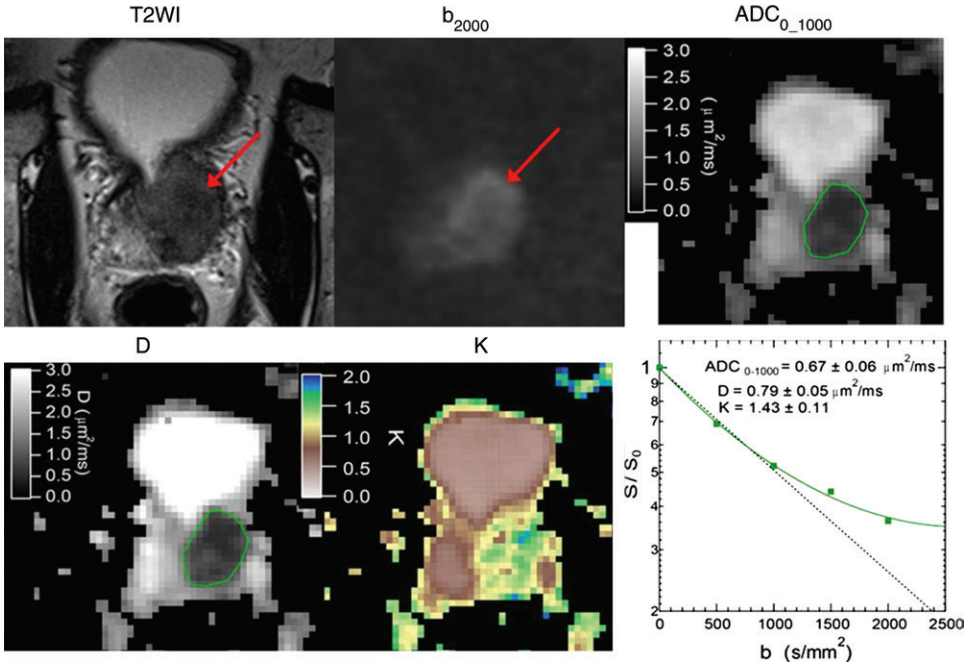

Figure 4: Prostate cancer. Images in a 58-year-old man with a large prostate lesion involving both the left peripheral and the transition zones (Gleason 4+4 tumor at biopsy). The panel shows the lesion on T2-weighted *(T2WI)* and diffusion-weighted, *b* value of 2000 sec/mm^2 *(b_{2000})* images (arrow), as well as ADC with combination of *b* values of 0, 1000 sec/mm^2 *($ADC_{0\text{-}1000}$)*, ADC_0 *(D)*, and kurtosis *(K)* maps. Signal plot shows the non-Gaussian diffusion curvature. (Image courtesy of Prof Andrew Rosenkrantz and Prof Eric Sigmund, New York University School of Medicine, New York, NY.)

evaluation of treatment efficacy, and prediction of disease recurrence.

Breast.—Accurate differential diagnosis of lesions, staging of malignant lesions, as well as monitoring of treatment efficacy, are essential in the treatment of breast cancer. The potential of diffusion MR imaging to address those questions is high, but results have been sometimes inconsistent in the literature partly due to differences in the study design (choice of *b* values and acquisition methods, data analysis approaches, differences in patient population). The majority of the clinical diffusion-weighted imaging breast studies rely on a monoexponential analysis, providing the simple ADC as the parameter analyzed. The combination of *b* values (0 and 1000 sec/mm^2), which include some non-Gaussian diffusion effects, seems to yield the highest diagnostic ability to differentiate benign from malignant lesions at 1.5 T (125). Some groups have attempted to extract both perfusion from IVIM and (Gaussian) diffusion components (126–128), leading to interesting results (Table E2 [online]). Recently, non-Gaussian diffusion has also been considered, giving promising results for the diagnosis of breast cancer (16,129,130), as diffusion kurtosis imaging parameters, in particular, may reflect physiologic and morphologic alterations associated with breast tumor tissues, although the mechanisms need to be elucidated (31). Kurtosis is high in malignant lesions compared with benign lesions and, in addition to ADC and flowing blood volume fraction, might improve diagnostic accuracy (16,129), for instance, combining parameter thresholds (131). Fibroadenomas and fibrocystic changes were found to have significant difference only in kurtosis (132). The flowing blood volume fraction is usually high in malignant lesions, but there seems to be a large overlap with benign lesions (Table E2 [online]). More complex architectural patterns are often present in complex fibroadenoma (with sclerosing adenosis or other components of fibrocystic change) (133) and complicated cysts, where flow patterns might erroneously result in an increase of the flowing blood volume fraction. Microscopic diffusion MR imaging of specimens with a resolution down to 40 μm might give new insights to the understanding of the microstructural complexity (134). A particularly challenging problem for breast diffusion MR imaging is the detection of non-mass-enhancing lesions on dynamic contrast-enhanced MR images. This appearance is typical of ductal carcinoma in situ due to the tumor extension along the breast ducts (135,136). Manual delineation of regions of interest is very time consuming, and there is a need for more automatic segmentation algorithms for diffusion MR imaging to be used in this clinical situation. Diffusion MR imaging has been evaluated in the

detection of lymphadenopathy in breast cancer; however, there is a significant overlap of ADC values between benign and malignant lymph nodes (137–141), and diffusion MR imaging cannot yet replace surgery and sentinel lymph node biopsy for lymph-node staging.

Lung.—The evaluation of lung nodules is frequently performed by using contrast-enhanced CT and FDG PET (142). Lung lesions have not been considered suitable for diffusion MR imaging due to severe susceptibility artifact from air. Nonetheless, recent developments in fast imaging methods such as echo-planar imaging and parallel imaging have now made this possible. Quantitative ADC measurements in lung cancer have been proposed to minimize the need of risky biopsies (143), and functional diffusion maps have been suggested to serve as a biomarker for early prediction of treatment response in non–small cell lung carcinoma, with a better performance than the conventional size criteria (Response Evaluation Criteria in Solid Tumors, or RECIST) (144). Still, to this date, the results have been conflicting or inconclusive (145,146).

Liver.—Detection and characterization of hepatocellular carcinoma and liver metastases, as well as prediction of tumor response to therapy, with MR imaging have benefited from liver-specific contrast agents (147,148). However, diffusion MR imaging has been actively investigated as an alternative approach in patients with severe renal failure (149). IVIM and diffusion MR imaging in the liver is degraded by artifacts due to cardiac and respiratory motion (150) or to air in the adjacent stomach or colon. Hence, work remains to be done to establish guidelines for the acquisition protocols (eg, free breathing or respiratory gating, navigation, etc) so as to obtain good image quality and reproducible IVIM and diffusion results (150–153). Interestingly, the first IVIM studies in the body were performed in the liver by Yamada et al in 1999 (154). They showed the potential of IVIM MR imaging to differentiate hepatocellular carcinoma, hemangioma, and cysts. Several studies have shown the potential of IVIM MR imaging for the evaluation of liver cirrhosis (155,156) or fibrosis (157), as well as for the tissue characterization of focal liver lesions (158). Combination of diffusion MR imaging and gadolinium ethoxybenzyl diethylenetriamine pentaacetic acid may increase sensitivity for the detection of hepatic lesions, including liver metastases (159–162). Still, use of ADC values solely for assessing hepatic lesions is likely to be challenging, as there is sometimes a considerable overlap between benign and malignant lesions and normal liver tissue (32,154,163,164).

Luciani et al (155) found that cirrhotic livers had significantly decreased ADC and IVIM pseudodiffusion coefficients compared with healthy livers, while the IVIM perfusion fraction has been shown as a potential biomarker of nonalcoholic steatohepatitis (165,166).

Other Clinical Applications

IVIM and diffusion MR imaging have also been used for a variety of other applications, each with its own challenges, such as organ motion for cardiac diffusion MR imaging and DTI (167,168). Diffusion MR imaging has the potential to differentiate benign from pathologic vertebral body compression fractures (169,170); however, large fat cells may reduce the negative correlation between tumor cellularity and ADC commonly found in most solid tumors (171). In the kidneys, IVIM parameters seem to be more useful than diffusion parameters with the potential to predict the extent of deterioration in renal function (172): D^* in the renal cortex is significantly lower in both mild and severe renal dysfunction, while ADC values decrease only in severe renal dysfunction. The perfusion fraction, fIVIM, and the tissue diffusivity have shown better diagnostic performance, separately, than the overall ADC for the discrimination of enhancing from nonenhancing renal lesions, with a good correlation between fIVIM and perfusion-related parameters using gadolinium-based contrast agents (173). Furthermore, histogram analyses of IVIM data have been shown useful for the discrimination of malignant and benign tumors, as well as renal tumor subtypes (174).

Future Prospects: Toward a Simplified, Quantitative Approach for Clinical Diffusion MR Imaging?

All those great applications have been a vibrant demonstration of the huge clinical potential of diffusion MR imaging, but it is particularly surprising to realize that many of those diffusion MR imaging "breakthroughs" have been based on empirical experimental evidence and have successfully moved into the clinical area with great success, but without a clear understanding of the mechanisms responsible for those findings. Water diffusion is modulated by cell size (decreasing with cell swelling, as observed in stroke), cell density (falling with the increase membrane content), or cell/membrane orientation (diffusion anisotropy in white matter fibers). But explanations for the observed findings have remained often qualitative. To better understand the basis of the observed findings in diffusion MR imaging, some physical modeling comes in as a necessity. Most models have focused on geometric features of tissues (eg, compartments such as the intra- and extracellular compartments, physical obstacles such as fibers, cell membranes). Undeniably cellular components are largely responsible for the reduced diffusion coefficients in biologic tissues compared with free water, and there is growing evidence that membranes, even if they are permeable, are likely the main actor that "hinders" the water diffusion process, directly or indirectly. However, data on the physical properties of water and on the status of water in biologic tissues suggest that the biophysical mechanisms of water diffusion in tissues may not be limited to sole geometric features (12). Beside protein-bounding, a large amount of water forms molecular networks through hydrogen bonding, with properties, including diffusion, which may also be altered in the vicinity of charged membranes. Given the important surface-to-volume ratio of

most cells, water networks interacting with cell membranes constitute an important fraction of tissue water. Hence, any change in cell component's shape, size, or density, which induces large variations in the membrane surface, will impact the diffusion MR imaging signal.

While it is very important to develop such sophisticated models, we should at the same time also make diffusion MR imaging as simple and robust as possible if one wants this outstanding modality to expand further in the clinics and become a standard, for instance, in oncology, as it is today with acute brain ischemia. The ADC concept has played such a role (14), but we should now also look at non-Gaussian diffusion and IVIM effects, as they provide valuable information on tissues. Unfortunately, the accurate estimation of such non-Gaussian diffusion and IVIM-related parameters requires fitting the diffusion-weighted MR imaging signal with biophysical models using algorithms, which are often prone to errors and calculation-intensive, preventing real-time analysis to be performed. Furthermore, accurate data fitting with models also requires the acquisition of multiple images with a large range of *b* values, resulting in long acquisition times. Ideally, one should aim at decreasing acquisition and processing times and at developing new, standard (across manufacturers' platforms) approaches that enable automatic classification of tissue types (ie, benign or malignant lesions) in real time.

Key *b* Value and Synthetic ADC Concepts

Previous literature has explored the optimization of *b* values in the kidney (175,176), liver (177,178), prostate (179), and the breast (180). However, those key *b* values have been proposed only to optimize the robustness of the fitting results in the context of the monoexponential model (Gaussian diffusion) or to separate IVIM and diffusion effects. A completely different approach would be to consider key *b* values directly aimed at differential diagnosis, taking into account altogether IVIM and non-Gaussian diffusion effects on the diffusion-weighted signal. Taking, for instance, the IVIM-kurtosis model, the signal intensity *S*(b) can be written (ignoring noise floor effects for the sake of simplicity) as (16):

$$S(\mathrm{b}) = S(0)\{\mathrm{fIVIM} \cdot \exp(-b \cdot D^*) + (1 - \mathrm{fIVIM}) \cdot \exp[-b \cdot \mathrm{ADC}_0 + (b \cdot \mathrm{ADC}_0)^2 \cdot K/6]\}, \quad (1)$$

where S(0) is the theoretical signal intensity for *b* value of 0 sec/mm^2, fIVIM is the (T1-, T2-weighted) volume fraction of incoherently flowing blood in the tissue, *b* is the *b* value, *D** is the pseudodiffusion coefficient associated with the IVIM effect, ADC_0 is the virtual ADC that would be obtained when *b* approaches 0, and *K* is the kurtosis parameter. As an example, using typical values for fIVIM, ADC_0, *K*, and *D** found for malignant and benign lesions in breast cancer (16), one can easily see (Fig 5, Fig E1 [online]) that the relative contribution to the signal intensity of each parameter strongly depends on the *b* values, as expected from Equation (1), but with a specific *b* value sensitivity. For instance, the most sensitive *b* values for fIVIM, *D**, ADC_0, and *K* are around 400, 200, 800, and above 3000 sec/mm^2, respectively. One can also see that *b* values between 1600 and 2400 sec/mm^2 are good both for ADC_0 and *K*. It also appears that variations in ADC_0 and *K* have a much greater impact on the overall signal intensity than variations in fIVIM and *D** (Fig 5), while at 400 sec/mm^2 IVIM and non-Gaussian diffusion effects cancel each other.

Based on this differential sensitivity, one may consider that some *b* values (we call "key *b* values") can be found to

Figure 5

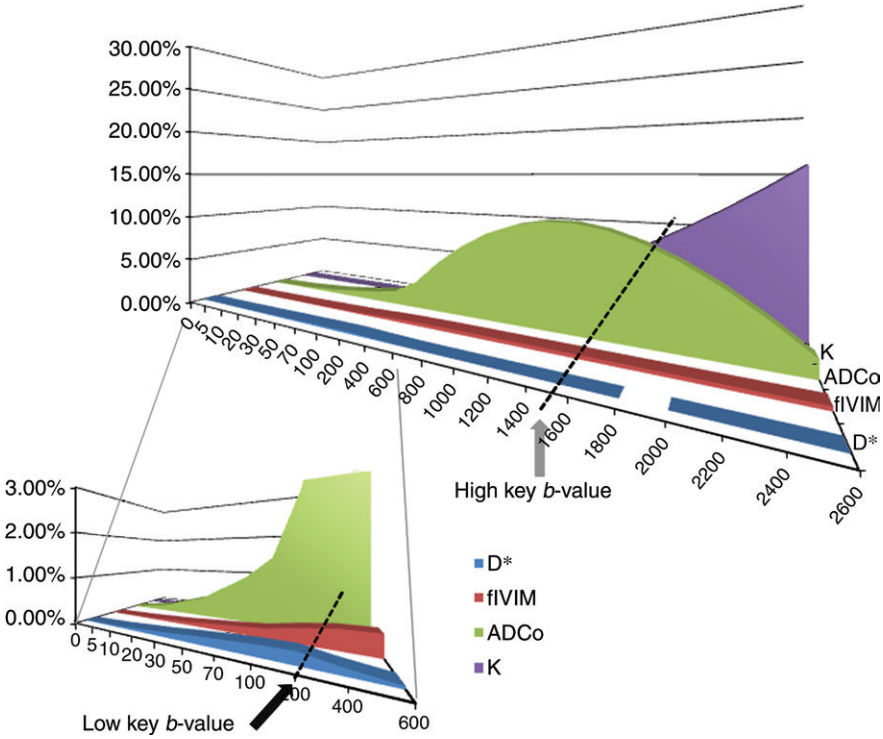

Figure 5: Differential sensitivity of the overall IVIM/diffusion signal to each parameter according to *b* value by using typical values shown in the table from reference 16. Low- and high-key *b* values can be identified to optimize sensitivity to IVIM (fIVIM and *D**) and to diffusion (virtual ADC that would be obtained when *b* approaches 0 *[ADC$_0$]* and kurtosis *[K]*) effects, respectively.

Figure 6

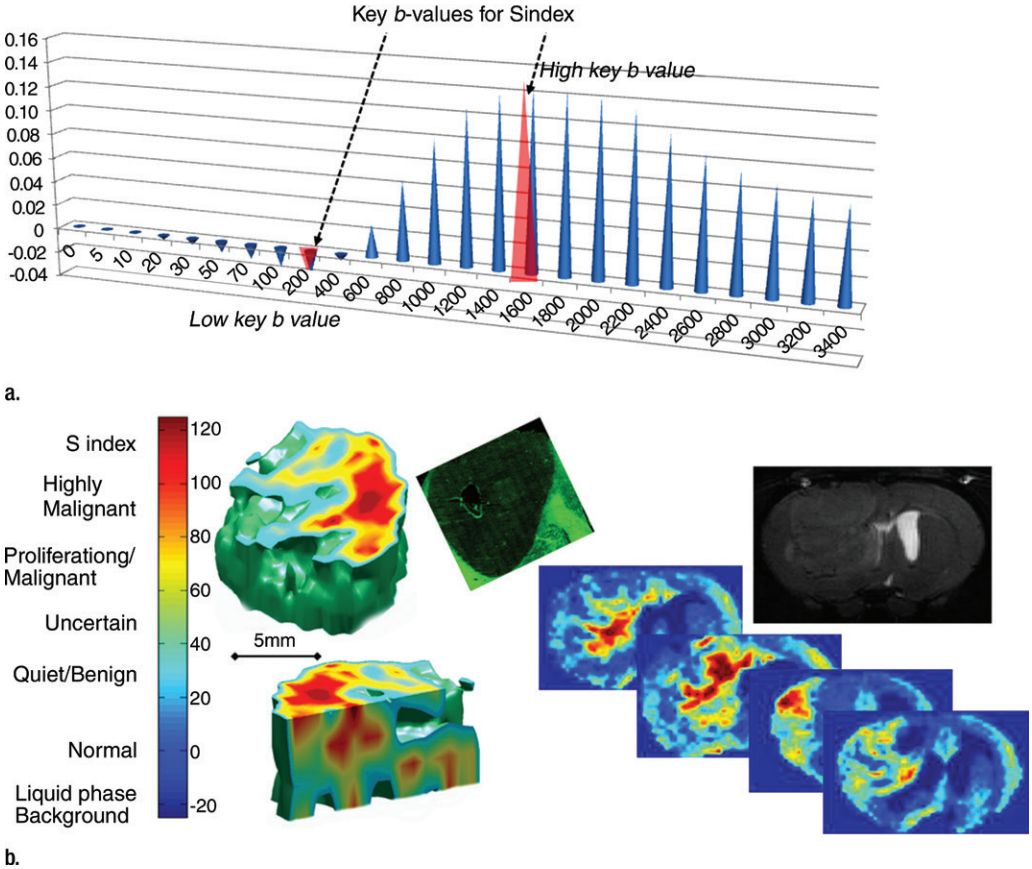

Figure 6: Sindex. **(a)** Combined sensitivity of diffusion-weighted MR imaging signal to all IVIM and diffusion parameters. **(b)** Using only the signal (voxel or region of interest level) acquired at the two key *b* values, an absolute Sindex can be derived that gives an indication on the tissue nature (color scale, left). The Sindex reflects the proximity of the lesion signal to the signal signature of typical tissues (eg, malignant, benign, liquid, etc). Example of Sindex maps (four sections) and three-dimensional rendering show tumor heterogeneity in a rat brain 9-L glioma tumor model. T2-weighted section and histologic slice (CD31 stain) are shown for reference (see reference 72 for experimental details).

maximize sensitivity to IVIM and diffusion parameters, hence to best distinguish tissues. Using the above values as an example, two key *b* values can be identified (Fig 6a): around 100–200 sec/mm^2 ("low" key *b* value, *Lb*) for IVIM and around 1400–1800 sec/mm^2 ("high" key *b* value, *Hb*) for non-Gaussian diffusion (mixing ADCo and kurtosis contributions). A *b* value above 3000 sec/mm^2 also has a strong tissue differentiation potential, but signal intensities acquired at such high *b* values generally become very low with the gradient hardware found on typical commercial MR imagers, and the kurtosis model is known to fail above such high *b* values.

In summary, optimal differentiation of tissue types could be obtained from only two *b* values (compared with many *b* values when the IVIM and diffusion parameters have to be evaluated individually), resulting in a dramatic shortening of the acquisition time, an important concern for clinical protocols, especially in noncooperative patients. Those two key *b* values are, of course, organ specific (eg, body vs brain), but, according to the existing literature, should be very similar for most body tissues.

Following the ADC concept introduced in the 1980s for Gaussian diffusion, which is calculated from two *b* values (0 and, for instance, 1000 sec/mm^2 for brain tissue), one may now define a synthetic ADC (sADC), which is calculated from those two key *b* values (eg, 200 and 1500 sec/mm^2) as follows:

$$\text{sADC} = \ln[S(\text{Lb})/S(\text{Hb})]/(\text{Hb} - \text{Lb}), \quad (2)$$

where Lb is low-key *b* value, Hb is high-key *b* value, and *S* is signal intensity. This synthetic ADC will intrinsically include non-Gaussian diffusion and IVIM effects in such a way as to maximize differential sensitivity to tissue structure.

"Sindex" Concept

One may go even one step further, directly identifying tissue types based on

their diffusion MR imaging signal patterns compared with signature signals, without the need to estimate any model parameter. Once those key *b* values have been identified, signature signals, $S_M(b)$ and $S_B(b)$, can be calculated at those *b* values, once for all, for instance by using Equation (1), for typical tissues (eg, malignant *[M]*, benign *[B]*, respectively). Taking now the normalized signals, $S_V(b)$, from a voxel (or region of interest) in a tissue under investigation at the key *b* values, a "distance" (algebraic distance, correlation coefficient, or scalar product, etc) can be calculated between the vector made of these tissue signals and those of the signature tissue signals using all key *b* values to build a quantitative, absolute signature index. In the simple case where only two key *b* values are used, as for the synthetic ADC, such a signature index, SI(V), can be defined as:

$$\begin{aligned} SI(V) = \max\{&[dS_V(Hb) \\ &- dS_V(Lb)]/[dS_M(Hb) \\ &- dS_M(Lb)],0\} \\ &- \max\{[dS_V(Hb) \\ &- dS_V(Lb)]/[dS_B(Hb) \\ &- dS_B(Lb)],0\}, \end{aligned} \quad (3)$$

where the relative "distance" quantities $dS_{V,M,B}(b) = [S_{V,M,B}(b) - S_N(b)]/S_N(b)$ are calculated between the signal of the tissue under investigation, S_V, the malignant, S_M, and the benign, S_B, tissue signals, and a reference neutral tissue signal, S_N (taken as an intermediate between malignant and benign signals). Because malignant lesions are characterized by high fIVIM, low ADCo, and high kurtosis values, one can see that for malignant tissues, the signature index is greater than 0 (1 for the typical malignant tissue of Fig 5), while it is less than 0 for benign tissues (−1 for the typical benign tissue of Fig 5). The signature index is 0 for a neutral (undetermined) tissue.

The signature index can further be linearly scaled, if needed, for convenience, for instance as Sindex = (SI + 1) × 25 + 25, which is now centered at 50, so that Sindex is 75 for a typical malignant tissue and 25 for a typical benign tissue. For normal tissues, the Sindex is approximately 0–20, while in very malignant tissues it is greater than 100 (Fig 6b). For example, based on results from a previously published breast study (16), the average Sindex was found to be 76 ± 34 in malignant lesions and 31 ± 34 in benign lesions. For a population of 46 patients with head and neck tumors, the overall performance (area under the receiver operating characteristic curve) of this Sindex to differentiate malignant from benign tumors was 0.89 (sensitivity, 89%; specificity, 84%; positive predictive value, 89%; and negative predictive value, 84%) (181).

In practice, this absolute scale Sindex derived from diffusion MR imaging signals acquired at only two key *b* values can be obtained at voxel level or within a manually or automatically drawn region of interest. Besides mean Sindex statistics in regions of interest, one may also generate histograms to assess lesion heterogeneity and monitor therapy response, for instance, by using the standard deviation or more advanced Sindex distribution descriptors, such as skewness or kurtosis, or determine a malignant charge by taking into account the lesion volume with voxels for which Sindex is greater than 50. Color-encoded maps and three-dimensional renderings of the lesions based on the voxel-by-voxel Sindex can also be generated for a better view of lesion conspicuity and heterogeneity or to provide spatial guidance for biopsy sites (181) (Fig 6b, Movie [online]).

As opposed to current approaches based on full fitting of MR imaging signals, which require iterative calculations using complex equations, the calculation of the Sindex is direct and straightforward (Eq [3]), making the processing time extremely short and compatible with real-time processing (Sindex results being obtained while the patient is still lying in the MR imaging scanner) and providing opportunities to perform additional scanning depending on the results. In short, tissues or lesions would be identified directly from their IVIM and diffusion MR imaging signal patterns without estimating any model parameter. This approach could facilitate the use of IVIM and diffusion MR imaging in the clinical field, especially for the monitoring (diagnosis and therapy assessment) of cancer lesions (68,87). Of course, those are concepts will have to be further developed and validated by using large patient cohorts involving various organs and lesion types.

In conclusion, IVIM and non-Gaussian diffusion MR imaging have the potential to give a semiautomatic diagnosis of lesions with high accuracy without using ionizing radiation and injection of radioisotopes or contrast agents. Once some stabilization has been reached in acquisition protocol designs and in the models and methods used for data processing, this approach has great potential not only to investigate neurologic and psychiatric disorders, but also in oncology for the diagnosis or staging of cancer lesions, as well as for drug development to evaluate response to therapy.

Acknowledgments: The authors thank the JSPS (Japan Society for the Promotion of Science) (MI) and the Louis D. and Louis Jeantet Foundations (DLB) for their generous support.

Disclosures of Conflicts of Interest: M.I. Activities related to the present article: disclosed no relevant relationships. Activities not related to the present article: received Grant-in-Aid for JSPS Fellows, Grant-in-Aid for Young Scientists (B), Kyoto University Hakubi grant. Other relationships: disclosed no relevant relationships. **D.L.B.** Activities related to the present article: disclosed no relevant relationships. Activities not related to the present article: disclosed no relevant relationships. Other relationships: author has a patent under consideration for Sindex.

References

1. Einstein A. Investigations on the theory of the Brownian movement. Mineola, NY: Courier Dover Publications, 1956.
2. Le Bihan D, Breton E, Lallemand D, Grenier P, Cabanis E, Laval-Jeantet M. MR imaging of intravoxel incoherent motions: application to diffusion and perfusion in neurologic disorders. Radiology 1986;161(2):401–407.
3. Le Bihan D. Intravoxel incoherent motion perfusion MR imaging: a wake-up call. Radiology 2008;249(3):748–752.
4. Takahara T, Imai Y, Yamashita T, Yasuda S, Nasu S, Van Cauteren M. Diffusion

weighted whole body imaging with background body signal suppression (DWIBS): technical improvement using free breathing, STIR and high resolution 3D display. Radiat Med 2004;22(4):275–282.

5. Perrin J. Mouvement brownien et réalité moléculaire. Ann Chim Phys 1909;18(8):5–114.
6. Le Bihan D, Johansen-Berg H. Diffusion MRI at 25: exploring brain tissue structure and function. Neuroimage 2012;61(2):324–341.
7. Le Bihan D, Mangin JF, Poupon C, et al. Diffusion tensor imaging: concepts and applications. J Magn Reson Imaging 2001;13(4):534–546.
8. Le Bihan D, Breton E. Imagerie de diffusion in-vivo par résonance magnétique nucléaire. C R Acad Sci (Paris) 1985;301(15):1109–1112.
9. Basser PJ, Mattiello J, LeBihan D. MR diffusion tensor spectroscopy and imaging. Biophys J 1994;66(1):259–267.
10. Eyal E, Shapiro-Feinberg M, Furman-Haran E, et al. Parametric diffusion tensor imaging of the breast. Invest Radiol 2012;47(5):284–291.
11. Notohamiprodjo M, Glaser C, Herrmann KA, et al. Diffusion tensor imaging of the kidney with parallel imaging: initial clinical experience. Invest Radiol 2008;43(10):677–685.
12. Le Bihan D. The 'wet mind': water and functional neuroimaging. Phys Med Biol 2007;52(7):R57–R90.
13. Yablonskiy DA, Sukstanskii AL. Theoretical models of the diffusion weighted MR signal. NMR Biomed 2010;23(7):661–681.
14. Le Bihan D. Apparent diffusion coefficient and beyond: what diffusion MR imaging can tell us about tissue structure. Radiology 2013;268(2):318–322.
15. Le Bihan D, Breton E, Lallemand D, Aubin ML, Vignaud J, Laval-Jeantet M. Separation of diffusion and perfusion in intravoxel incoherent motion MR imaging. Radiology 1988;168(2):497–505.
16. Iima M, Yano K, Kataoka M, et al. Quantitative non-Gaussian diffusion and intravoxel incoherent motion magnetic resonance imaging: differentiation of malignant and benign breast lesions. Invest Radiol 2015;50(4):205–211.
17. Dixon WT. Separation of diffusion and perfusion in intravoxel incoherent motion MR imaging: a modest proposal with tremendous potential. Radiology 1988;168(2):566–567.
18. High WA, Ayers RA, Cowper SE. Gadolinium is quantifiable within the tissue of patients with nephrogenic systemic fibrosis. J Am Acad Dermatol 2007;56(4):710–712.
19. ACR Manual on Contrast Media. http://www.acr.org/~/media/ACR/Documents/PDF/QualitySafety/Resources/Contrast%20Manual/2013_Contrast_Media.pdf. Published 2013. Accessed May 15, 2015.
20. Kanda T, Ishii K, Kawaguchi H, Kitajima K, Takenaka D. High signal intensity in the dentate nucleus and globus pallidus on unenhanced T1-weighted MR images: relationship with increasing cumulative dose of a gadolinium-based contrast material. Radiology 2014;270(3):834–841.
21. Notohamiprodjo M, Chandarana H, Mikheev A, et al. Combined intravoxel incoherent motion and diffusion tensor imaging of renal diffusion and flow anisotropy. Magn Reson Med 2015;73(4):1526–1532.
22. Pyatigorskaya N, Le Bihan D, Reynaud O, Ciobanu L. Relationship between the diffusion time and the diffusion MRI signal observed at 17.2 Tesla in the healthy rat brain cortex. Magn Reson Med 2014;72(2):492–500.
23. McNab JA, Edlow BL, Witzel T, et al. The Human Connectome Project and beyond: initial applications of 300 mT/m gradients. Neuroimage 2013;80:234–245.
24. Chabert S, Meca C, Le Bihan D. Relevance of the information about the diffusion distribution in vivo given by kurtosis in q-space imaging [abstr]. In: Proceedings of the Twelfth Meeting of the International Society for Magnetic Resonance in Medicine. Berkeley, Calif: International Society for Magnetic Resonance in Medicine, 2004;1238.
25. Jensen JH, Helpern JA, Ramani A, Lu H, Kaczynski K. Diffusional kurtosis imaging: the quantification of non-gaussian water diffusion by means of magnetic resonance imaging. Magn Reson Med 2005;53(6):1432–1440.
26. Mulkern RV, Haker SJ, Maier SE. On high b diffusion imaging in the human brain: ruminations and experimental insights. Magn Reson Imaging 2009;27(8):1151–1162.
27. Yablonskiy DA, Bretthorst GL, Ackerman JJ. Statistical model for diffusion attenuated MR signal. Magn Reson Med 2003;50(4):664–669.
28. Bennett KM, Schmainda KM, Bennett RT, Rowe DB, Lu H, Hyde JS. Characterization of continuously distributed cortical water diffusion rates with a stretched-exponential model. Magn Reson Med 2003;50(4):727–734.
29. Hall MG, Barrick TR. From diffusion-weighted MRI to anomalous diffusion imaging. Magn Reson Med 2008;59(3):447–455.
30. Zhou XJ, Gao Q, Abdullah O, Magin RL. Studies of anomalous diffusion in the human brain using fractional order calculus. Magn Reson Med 2010;63(3):562–569.
31. Grinberg F, Farrher E, Ciobanu L, Geffroy F, Le Bihan D, Shah NJ. Non-Gaussian diffusion imaging for enhanced contrast of brain tissue affected by ischemic stroke. PLoS One 2014;9(2):e89225.
32. Anderson SW, Barry B, Soto J, Ozonoff A, O'Brien M, Jara H. Characterizing non-gaussian, high b-value diffusion in liver fibrosis: stretched exponential and diffusional kurtosis modeling. J Magn Reson Imaging 2014;39(4):827–834.
33. Yuan J, Yeung DK, Mok GS, et al. Non-Gaussian analysis of diffusion weighted imaging in head and neck at 3T: a pilot study in patients with nasopharyngeal carcinoma. PLoS One 2014;9(1):e87024.
34. Filli L, Wurnig M, Nanz D, Luechinger R, Kenkel D, Boss A. Whole-body diffusion kurtosis imaging: initial experience on non-Gaussian diffusion in various organs. Invest Radiol 2014;49(12):773–778.
35. Assaf Y, Basser PJ. Composite hindered and restricted model of diffusion (CHARMED) MR imaging of the human brain. Neuroimage 2005;27(1):48–58.
36. Assaf Y, Blumenfeld-Katzir T, Yovel Y, Basser PJ. AxCaliber: a method for measuring axon diameter distribution from diffusion MRI. Magn Reson Med 2008;59(6):1347–1354.
37. Zhang H, Schneider T, Wheeler-Kingshott CA, Alexander DC. NODDI: practical in vivo neurite orientation dispersion and density imaging of the human brain. Neuroimage 2012;61(4):1000–1016.
38. Gudbjartsson H, Patz S. The Rician distribution of noisy MRI data. Magn Reson Med 1995;34(6):910–914.
39. Aja-Fernández S, Tristán-Vega A, Hoge WS. Statistical noise analysis in GRAPPA using a parametrized noncentral Chi approximation model. Magn Reson Med 2011;65(4):1195–1206.
40. Brion V, Poupon C, Riff O, et al. Parallel MRI noise correction: an extension of the LMMSE to non central chi distributions. Med Image Comput Comput Assist Interv 2011;14(Pt 2):226–233.
41. Constantinides CD, Atalar E, McVeigh ER. Signal-to-noise measurements in magnitude images from NMR phased arrays. Magn Reson Med 1997;38(5):852–857.

42. Koay CG, Basser PJ. Analytically exact correction scheme for signal extraction from noisy magnitude MR signals. J Magn Reson 2006;179(2):317–322.

43. Tofts PS, Lloyd D, Clark CA, et al. Test liquids for quantitative MRI measurements of self-diffusion coefficient in vivo. Magn Reson Med 2000;43(3):368–374.

44. Moseley ME, Cohen Y, Mintorovitch J, et al. Early detection of regional cerebral ischemia in cats: comparison of diffusion- and T2-weighted MRI and spectroscopy. Magn Reson Med 1990;14(2):330–346.

45. Schlaug G, Siewert B, Benfield A, Edelman RR, Warach S. Time course of the apparent diffusion coefficient (ADC) abnormality in human stroke. Neurology 1997; 49(1):113–119.

46. Sotak CH. The role of diffusion tensor imaging in the evaluation of ischemic brain injury - a review. NMR Biomed 2002;15(7-8): 561–569.

47. Norris DG, Niendorf T, Leibfritz D. Health and infarcted brain tissues studied at short diffusion times: the origins of apparent restriction and the reduction in apparent diffusion coefficient. NMR Biomed 1994;7(7):304–310.

48. Warach S, Boska M, Welch KM. Pitfalls and potential of clinical diffusion-weighted MR imaging in acute stroke. Stroke 1997; 28(3):481–482.

49. Warach S, Dashe JF, Edelman RR. Clinical outcome in ischemic stroke predicted by early diffusion-weighted and perfusion magnetic resonance imaging: a preliminary analysis. J Cereb Blood Flow Metab 1996;16(1):53–59.

50. Lövblad KO, Baird AE, Schlaug G, et al. Ischemic lesion volumes in acute stroke by diffusion-weighted magnetic resonance imaging correlate with clinical outcome. Ann Neurol 1997;42(2):164–170.

51. González RG, Schaefer PW, Buonanno FS, et al. Diffusion-weighted MR imaging: diagnostic accuracy in patients imaged within 6 hours of stroke symptom onset. Radiology 1999;210(1):155–162.

52. Dreher W, Kühn B, Gyngell ML, et al. Temporal and regional changes during focal ischemia in rat brain studied by proton spectroscopic imaging and quantitative diffusion NMR imaging. Magn Reson Med 1998; 39(6):878–888.

53. Cheung JS, Wang E, Lo EH, Sun PZ. Stratification of heterogeneous diffusion MRI ischemic lesion with kurtosis imaging: evaluation of mean diffusion and kurtosis MRI mismatch in an animal model of transient focal ischemia. Stroke 2012;43(8):2252–2254.

54. Federau C, Sumer S, Becce F, et al. Intravoxel incoherent motion perfusion imaging in acute stroke: initial clinical experience. Neuroradiology 2014;56(8):629–635.

55. Federau C, Hagmann P, Maeder P, et al. Dependence of brain intravoxel incoherent motion perfusion parameters on the cardiac cycle. PLoS One 2013;8(8):e72856.

56. Nimsky C, Ganslandt O, Hastreiter P, et al. Preoperative and intraoperative diffusion tensor imaging-based fiber tracking in glioma surgery. Neurosurgery 2005;56(1): 130–137; discussion 138.

57. Shizukuishi T, Abe O, Aoki S. Diffusion tensor imaging analysis for psychiatric disorders. Magn Reson Med Sci 2013;12(3): 153–159.

58. Rovaris M, Gass A, Bammer R, et al. Diffusion MRI in multiple sclerosis. Neurology 2005;65(10):1526–1532.

59. Balasubramanya KS, Kovoor JM, Jayakumar PN, et al. Diffusion-weighted imaging and proton MR spectroscopy in the characterization of acute disseminated encephalomyelitis. Neuroradiology 2007; 49(2):177–183.

60. Balashov KE, Aung LL, Dhib-Jalbut S, Keller IA. Acute multiple sclerosis lesion: conversion of restricted diffusion due to vasogenic edema. J Neuroimaging 2011;21(2): 202–204.

61. Bodini B, Cercignani M, Khaleeli Z, et al. Corpus callosum damage predicts disability progression and cognitive dysfunction in primary-progressive MS after five years. Hum Brain Mapp 2013;34(5):1163–1172.

62. Rueda Lopes FC, Doring T, Martins C, et al. The role of demyelination in neuromyelitis optica damage: diffusion-tensor MR imaging study. Radiology 2012;263(1):235–242.

63. Shenton ME, Hamoda HM, Schneiderman JS, et al. A review of magnetic resonance imaging and diffusion tensor imaging findings in mild traumatic brain injury. Brain Imaging Behav 2012;6(2):137–192.

64. Alhilali LM, Yaeger K, Collins M, Fakhran S. Detection of central white matter injury underlying vestibulopathy after mild traumatic brain injury. Radiology 2014; 272(1):224–232.

65. Chong CD, Schwedt TJ. White matter damage and brain network alterations in concussed patients: a review of recent diffusion tensor imaging and resting-state functional connectivity data. Curr Pain Headache Rep 2015;19(5):485.

66. Patterson DM, Padhani AR, Collins DJ. Technology insight: water diffusion MRI—a potential new biomarker of response to cancer therapy. Nat Clin Pract Oncol 2008;5(4):220–233.

67. Toledano-Massiah S, Luciani A, Itti E, et al. Whole-body diffusion-weighted imaging in Hodgkin lymphoma and diffuse large B-cell lymphoma. RadioGraphics 2015; 35(3):747–764.

68. Padhani AR, Liu G, Koh DM, et al. Diffusion-weighted magnetic resonance imaging as a cancer biomarker: consensus and recommendations. Neoplasia 2009;11(2):102–125.

69. Guo Y, Cai YQ, Cai ZL, et al. Differentiation of clinically benign and malignant breast lesions using diffusion-weighted imaging. J Magn Reson Imaging 2002;16(2):172–178.

70. Sugahara T, Korogi Y, Kochi M, et al. Usefulness of diffusion-weighted MRI with echo-planar technique in the evaluation of cellularity in gliomas. J Magn Reson Imaging 1999;9(1):53–60.

71. Humphries PD, Sebire NJ, Siegel MJ, Olsen ØE. Tumors in pediatric patients at diffusion-weighted MR imaging: apparent diffusion coefficient and tumor cellularity. Radiology 2007;245(3):848–854.

72. Iima M, Reynaud O, Tsurugizawa T, et al. Characterization of glioma microcirculation and tissue features using intravoxel incoherent motion magnetic resonance imaging in a rat brain model. Invest Radiol 2014;49(7):485–490.

73. Fan G, Zang P, Jing F, Wu Z, Guo Q. Usefulness of diffusion/perfusion-weighted MRI in rat gliomas: correlation with histopathology. Acad Radiol 2005;12(5):640–651.

74. Turkbey B, Shah VP, Pang Y, et al. Is apparent diffusion coefficient associated with clinical risk scores for prostate cancers that are visible on 3-T MR images? Radiology 2011;258(2):488–495.

75. Nakajo M, Kajiya Y, Kaneko T, et al. FDG PET/CT and diffusion-weighted imaging for breast cancer: prognostic value of maximum standardized uptake values and apparent diffusion coefficient values of the primary lesion. Eur J Nucl Med Mol Imaging 2010;37(11):2011–2020.

76. Koh DM, Scurr E, Collins D, et al. Predicting response of colorectal hepatic metastasis: value of pretreatment apparent diffusion coefficients. AJR Am J Roentgenol 2007;188(4):1001–1008.

77. Cui Y, Zhang XP, Sun YS, Tang L, Shen L. Apparent diffusion coefficient: potential imaging biomarker for prediction and

early detection of response to chemotherapy in hepatic metastases. Radiology 2008; 248(3):894–900.

78. Sun YS, Zhang XP, Tang L, et al. Locally advanced rectal carcinoma treated with preoperative chemotherapy and radiation therapy: preliminary analysis of diffusion-weighted MR imaging for early detection of tumor histopathologic downstaging. Radiology 2010;254(1):170–178.
79. Yabuuchi H, Soeda H, Matsuo Y, et al. Phyllodes tumor of the breast: correlation between MR findings and histologic grade. Radiology 2006;241(3):702–709.
80. Higano S, Yun X, Kumabe T, et al. Malignant astrocytic tumors: clinical importance of apparent diffusion coefficient in prediction of grade and prognosis. Radiology 2006; 241(3):839–846.
81. Lee HJ, Rha SY, Chung YE, et al. Tumor perfusion-related parameter of diffusion-weighted magnetic resonance imaging: correlation with histological microvessel density. Magn Reson Med 2014;71(4): 1554–1558.
82. Federau C, Meuli R, O'Brien K, Maeder P, Hagmann P. Perfusion measurement in brain gliomas with intravoxel incoherent motion MRI. AJNR Am J Neuroradiol 2014;35(2):256–262.
83. Kim HS, Suh CH, Kim N, Choi CG, Kim SJ. Histogram analysis of intravoxel incoherent motion for differentiating recurrent tumor from treatment effect in patients with glioblastoma: initial clinical experience. AJNR Am J Neuroradiol 2014;35(3): 490–497.
84. Chandarana H, Kang SK, Wong S, et al. Diffusion-weighted intravoxel incoherent motion imaging of renal tumors with histopathologic correlation. Invest Radiol 2012;47(12):688–696.
85. Fujima N, Yoshida D, Sakashita T, et al. Intravoxel incoherent motion diffusion-weighted imaging in head and neck squamous cell carcinoma: assessment of perfusion-related parameters compared to dynamic contrast-enhanced MRI. Magn Reson Imaging 2014;32(10):1206–1213.
86. Suo S, Lin N, Wang H, et al. Intravoxel incoherent motion diffusion-weighted MR imaging of breast cancer at 3.0 tesla: comparison of different curve-fitting methods. J Magn Reson Imaging 2015;42(2):362–370.
87. Padhani AR, Koh DM, Collins DJ. Whole-body diffusion-weighted MR imaging in cancer: current status and research directions. Radiology 2011;261(3):700–718.
88. Yamasaki F, Kurisu K, Satoh K, et al. Apparent diffusion coefficient of human brain tumors at MR imaging. Radiology 2005;235(3):985–991.
89. Bulakbasi N, Guvenc I, Onguru O, Erdogan E, Tayfun C, Ucoz T. The added value of the apparent diffusion coefficient calculation to magnetic resonance imaging in the differentiation and grading of malignant brain tumors. J Comput Assist Tomogr 2004; 28(6):735–746.
90. Assaf Y, Pasternak O. Diffusion tensor imaging (DTI)-based white matter mapping in brain research: a review. J Mol Neurosci 2008;34(1):51–61.
91. Chenevert TL, Stegman LD, Taylor JM, et al. Diffusion magnetic resonance imaging: an early surrogate marker of therapeutic efficacy in brain tumors. J Natl Cancer Inst 2000;92(24):2029–2036.
92. Hamstra DA, Chenevert TL, Moffat BA, et al. Evaluation of the functional diffusion map as an early biomarker of time-to-progression and overall survival in high-grade glioma. Proc Natl Acad Sci U S A 2005; 102(46):16759–16764.
93. Hu YC, Yan LF, Wu L, et al. Intravoxel incoherent motion diffusion-weighted MR imaging of gliomas: efficacy in preoperative grading. Sci Rep 2014;4:7208.
94. Zulfiqar M, Yousem DM, Lai H. ADC values and prognosis of malignant astrocytomas: does lower ADC predict a worse prognosis independent of grade of tumor?—a meta-analysis. AJR Am J Roentgenol 2013; 200(3):624–629.
95. Waldman AD, Jackson A, Price SJ, et al. Quantitative imaging biomarkers in neuro-oncology. Nat Rev Clin Oncol 2009;6(8): 445–454.
96. Thoeny HC, De Keyzer F, King AD. Diffusion-weighted MR imaging in the head and neck. Radiology 2012;263(1):19–32.
97. Koyasu S, Iima M, Umeoka S, et al. The clinical utility of reduced-distortion readout-segmented echo-planar imaging in the head and neck region: initial experience. Eur Radiol 2014;24(12):3088–3096.
98. Sumi M, Van Cauteren M, Sumi T, Obara M, Ichikawa Y, Nakamura T. Salivary gland tumors: use of intravoxel incoherent motion MR imaging for assessment of diffusion and perfusion for the differentiation of benign from malignant tumors. Radiology 2012;263(3):770–777.
99. Sumi M, Nakamura T. Head and neck tumours: combined MRI assessment based on IVIM and TIC analyses for the differentiation of tumors of different histological types. Eur Radiol 2014;24(1):223–231.
100. Sumi M, Nakamura T. Head and neck tumors: assessment of perfusion-related parameters and diffusion coefficients based on the intravoxel incoherent motion model. AJNR Am J Neuroradiol 2013;34(2):410–416.
101. Vandecaveye V, De Keyzer F, Vander Poorten V, et al. Head and neck squamous cell carcinoma: value of diffusion-weighted MR imaging for nodal staging. Radiology 2009; 251(1):134–146.
102. Lu Y, Jansen JF, Stambuk HE, et al. Comparing primary tumors and metastatic nodes in head and neck cancer using intravoxel incoherent motion imaging: a preliminary experience. J Comput Assist Tomogr 2013;37(3):346–352.
103. Kim S, Loevner L, Quon H, et al. Diffusion-weighted magnetic resonance imaging for predicting and detecting early response to chemoradiation therapy of squamous cell carcinomas of the head and neck. Clin Cancer Res 2009;15(3):986–994.
104. Vandecaveye V, Dirix P, De Keyzer F, et al. Diffusion-weighted magnetic resonance imaging early after chemoradiotherapy to monitor treatment response in head-and-neck squamous cell carcinoma. Int J Radiat Oncol Biol Phys 2012;82(3): 1098–1107.
105. Tshering Vogel DW, Zbaeren P, Geretschlaeger A, Vermathen P, De Keyzer F, Thoeny HC. Diffusion-weighted MR imaging including bi-exponential fitting for the detection of recurrent or residual tumour after (chemo)radiotherapy for laryngeal and hypopharyngeal cancers. Eur Radiol 2013;23(2):562–569.
106. Barral M, Taouli B, Guiu B, et al. Diffusion-weighted MR imaging of the pancreas: current status and recommendations. Radiology 2015;274(1):45–63.
107. Lee SS, Byun JH, Park BJ, et al. Quantitative analysis of diffusion-weighted magnetic resonance imaging of the pancreas: usefulness in characterizing solid pancreatic masses. J Magn Reson Imaging 2008; 28(4):928–936.
108. Re TJ, Lemke A, Klauss M, et al. Enhancing pancreatic adenocarcinoma delineation in diffusion derived intravoxel incoherent motion f-maps through automatic vessel and duct segmentation. Magn Reson Med 2011;66(5):1327–1332.
109. Klauss M, Lemke A, Grünberg K, et al. Intravoxel incoherent motion MRI for the differentiation between mass forming chronic pancreatitis and pancreatic carcinoma. Invest Radiol 2011;46(1):57–63.

110. Concia M, Sprinkart AM, Penner AH, et al. Diffusion-weighted magnetic resonance imaging of the pancreas: diagnostic benefit from an intravoxel incoherent motion model-based 3 b-value analysis. Invest Radiol 2014;49(2):93–100.

111. Kang KM, Lee JM, Yoon JH, Kiefer B, Han JK, Choi BI. Intravoxel incoherent motion diffusion-weighted MR imaging for characterization of focal pancreatic lesions. Radiology 2014;270(2):444–453.

112. Johnson LM, Turkbey B, Figg WD, Choyke PL. Multiparametric MRI in prostate cancer management. Nat Rev Clin Oncol 2014;11(6):346–353.

113. Rosenkrantz AB, Sigmund EE, Johnson G, et al. Prostate cancer: feasibility and preliminary experience of a diffusional kurtosis model for detection and assessment of aggressiveness of peripheral zone cancer. Radiology 2012;264(1):126–135.

114. Mazzoni LN, Lucarini S, Chiti S, Busoni S, Gori C, Menchi I. Diffusion-weighted signal models in healthy and cancerous peripheral prostate tissues: comparison of outcomes obtained at different b-values. J Magn Reson Imaging 2014;39(3):512–518.

115. Shinmoto H, Oshio K, Tanimoto A, et al. Biexponential apparent diffusion coefficients in prostate cancer. Magn Reson Imaging 2009;27(3):355–359.

116. Shinmoto H, Oshio K, Tamura C, et al. Diffusion-weighted imaging of prostate cancer using a statistical model based on the gamma distribution. J Magn Reson Imaging 2015;42(1):56–62.

117. Kuru TH, Roethke MC, Stieltjes B, et al. Intravoxel incoherent motion (IVIM) diffusion imaging in prostate cancer: what does it add? J Comput Assist Tomogr 2014;38(4):558–564.

118. Pang Y, Turkbey B, Bernardo M, et al. Intravoxel incoherent motion MR imaging for prostate cancer: an evaluation of perfusion fraction and diffusion coefficient derived from different b-value combinations. Magn Reson Med 2013;69(2):553–562.

119. Zhang YD, Wang Q, Wu CJ, et al. The histogram analysis of diffusion-weighted intravoxel incoherent motion (IVIM) imaging for differentiating the gleason grade of prostate cancer. Eur Radiol 2015;25(4):994–1004.

120. Anderson AW, Gore JC. Analysis and correction of motion artifacts in diffusion weighted imaging. Magn Reson Med 1994;32(3):379–387.

121. Döpfert J, Lemke A, Weidner A, Schad LR. Investigation of prostate cancer using diffusion-weighted intravoxel incoherent motion imaging. Magn Reson Imaging 2011;29(8):1053–1058.

122. Mazaheri Y, Vargas HA, Akin O, Goldman DA, Hricak H. Reducing the influence of b-value selection on diffusion-weighted imaging of the prostate: evaluation of a revised monoexponential model within a clinical setting. J Magn Reson Imaging 2012;35(3):660–668.

123. Riches SF, Hawtin K, Charles-Edwards EM, de Souza NM. Diffusion-weighted imaging of the prostate and rectal wall: comparison of biexponential and monoexponential modelled diffusion and associated perfusion coefficients. NMR Biomed 2009;22(3):318–325.

124. Shinmoto H, Tamura C, Soga S, et al. An intravoxel incoherent motion diffusion-weighted imaging study of prostate cancer. AJR Am J Roentgenol 2012;199(4):W496–W500.

125. Dorrius MD, Dijkstra H, Oudkerk M, Sijens PE. Effect of b value and pre-admission of contrast on diagnostic accuracy of 1.5-T breast DWI: a systematic review and meta-analysis. Eur Radiol 2014;24(11):2835–2847.

126. Liu C, Liang C, Liu Z, Zhang S, Huang B. Intravoxel incoherent motion (IVIM) in evaluation of breast lesions: comparison with conventional DWI. Eur J Radiol 2013;82(12):e782–e789.

127. Bokacheva L, Kaplan JB, Giri DD, et al. Intravoxel incoherent motion diffusion-weighted MRI at 3.0 T differentiates malignant breast lesions from benign lesions and breast parenchyma. J Magn Reson Imaging 2014;40(4):813–823.

128. Sigmund EE, Cho GY, Kim S, et al. Intravoxel incoherent motion imaging of tumor microenvironment in locally advanced breast cancer. Magn Reson Med 2011;65(5):1437–1447.

129. Wu D, Li G, Zhang J, Chang S, Hu J, Dai Y. Characterization of breast tumors using diffusion kurtosis imaging (DKI). PLoS One 2014;9(11):e113240.

130. Tamura T, Usui S, Murakami S, et al. Biexponential signal attenuation analysis of diffusion-weighted imaging of breast. Magn Reson Med Sci 2010;9(4):195–207.

131. Iima M, Kataoka M, Umehana M, et al. Computer-assisted diagnosis of breast lesions based on IVIM and non Gaussian diffusion MRI [abstr]. In: Proceedings of the Twenty-Second Meeting of the International Society for Magnetic Resonance in Medicine. Berkeley, Calif: International Society for Magnetic Resonance in Medicine, 2014.

132. Nogueira L, Brandão S, Matos E, et al. Application of the diffusion kurtosis model for the study of breast lesions. Eur Radiol 2014;24(6):1197–1203.

133. Rosen PP. Rosen's breast pathology. Philadelphia, Pa: Lippincott Williams & Wilkins, 2009; 194–195.

134. Norddin N, Power C, Watson G, et al. Microscopic diffusion properties of fixed breast tissue: preliminary findings. Magn Reson Med 2014 Dec 17. [Epub ahead of print]

135. Cheng L, Bai Y, Zhang J, et al. Optimization of apparent diffusion coefficient measured by diffusion-weighted MRI for diagnosis of breast lesions presenting as mass and non-mass-like enhancement. Tumour Biol 2013;34(3):1537–1545.

136. Iima M, Le Bihan D, Okumura R, et al. Apparent diffusion coefficient as an MR imaging biomarker of low-risk ductal carcinoma in situ: a pilot study. Radiology 2011;260(2):364–372.

137. Kwee TC, Takahara T, Luijten PR, Nievelstein RA. ADC measurements of lymph nodes: inter- and intra-observer reproducibility study and an overview of the literature. Eur J Radiol 2010;75(2):215–220.

138. Scaranelo AM, Eiada R, Jacks LM, Kulkarni SR, Crystal P. Accuracy of unenhanced MR imaging in the detection of axillary lymph node metastasis: study of reproducibility and reliability. Radiology 2012;262(2):425–434.

139. Fornasa F, Nesoti MV, Bovo C, Bonavina MG. Diffusion-weighted magnetic resonance imaging in the characterization of axillary lymph nodes in patients with breast cancer. J Magn Reson Imaging 2012;36(4):858–864.

140. Kamitani T, Hatakenaka M, Yabuuchi H, et al. Detection of axillary node metastasis using diffusion-weighted MRI in breast cancer. Clin Imaging 2013;37(1):56–61.

141. Luo N, Su D, Jin G, et al. Apparent diffusion coefficient ratio between axillary lymph node with primary tumor to detect nodal metastasis in breast cancer patients. J Magn Reson Imaging 2013;38(4):824–828.

142. Gould MK, Fletcher J, Iannettoni MD, et al. Evaluation of patients with pulmonary nodules: when is it lung cancer?: ACCP evidence-based clinical practice guidelines (2nd edition). Chest 2007;132(3 Suppl):108S–130S.

143. Liu H, Liu Y, Yu T, Ye N, Wang Q. Evaluation of apparent diffusion coefficient

associated with pathological grade of lung carcinoma, before therapy. J Magn Reson Imaging 2014 Dec 24. [Epub ahead of print]

144. Reischauer C, Froehlich JM, Pless M, Binkert CA, Koh DM, Gutzeit A. Early treatment response in non-small cell lung cancer patients using diffusion-weighted imaging and functional diffusion maps: a feasibility study. PLoS One 2014;9(10):e108052.

145. Chen L, Zhang J, Bao J, et al. Meta-analysis of diffusion-weighted MRI in the differential diagnosis of lung lesions. J Magn Reson Imaging 2013;37(6):1351–1358.

146. Li B, Li Q, Chen C, Guan Y, Liu S. A systematic review and meta-analysis of the accuracy of diffusion-weighted MRI in the detection of malignant pulmonary nodules and masses. Acad Radiol 2014;21(1):21–29.

147. Halavaara J, Breuer J, Ayuso C, et al. Liver tumor characterization: comparison between liver-specific gadoxetic acid disodium-enhanced MRI and biphasic CT—a multicenter trial. J Comput Assist Tomogr 2006;30(3):345–354.

148. Bipat S, van Leeuwen MS, Comans EF, et al. Colorectal liver metastases: CT, MR imaging, and PET for diagnosis—meta-analysis. Radiology 2005;237(1):123–131.

149. Koh DM, Collins DJ. Diffusion-weighted MRI in the body: applications and challenges in oncology. AJR Am J Roentgenol 2007;188(6):1622–1635.

150. Lee Y, Lee SS, Kim N, et al. Intravoxel incoherent motion diffusion-weighted MR imaging of the liver: effect of triggering methods on regional variability and measurement repeatability of quantitative parameters. Radiology 2015;274(2):405–415.

151. Taouli B, Sandberg A, Stemmer A, et al. Diffusion-weighted imaging of the liver: comparison of navigator triggered and breathhold acquisitions. J Magn Reson Imaging 2009;30(3):561–568.

152. Kandpal H, Sharma R, Madhusudhan KS, Kapoor KS. Respiratory-triggered versus breath-hold diffusion-weighted MRI of liver lesions: comparison of image quality and apparent diffusion coefficient values. AJR Am J Roentgenol 2009;192(4):915–922.

153. Chen X, Qin L, Pan D, et al. Liver diffusion-weighted MR imaging: reproducibility comparison of ADC measurements obtained with multiple breath-hold, free-breathing, respiratory-triggered, and navigator-triggered techniques. Radiology 2014;271(1):113–125.

154. Yamada I, Aung W, Himeno Y, Nakagawa T, Shibuya H. Diffusion coefficients in abdominal organs and hepatic lesions: evaluation with intravoxel incoherent motion echo-planar MR imaging. Radiology 1999;210(3):617–623.

155. Luciani A, Vignaud A, Cavet M, et al. Liver cirrhosis: intravoxel incoherent motion MR imaging—pilot study. Radiology 2008;249(3):891–899.

156. Patel J, Sigmund EE, Rusinek H, Oei M, Babb JS, Taouli B. Diagnosis of cirrhosis with intravoxel incoherent motion diffusion MRI and dynamic contrast-enhanced MRI alone and in combination: preliminary experience. J Magn Reson Imaging 2010;31(3):589–600.

157. Dyvorne HA, Galea N, Nevers T, et al. Diffusion-weighted imaging of the liver with multiple b values: effect of diffusion gradient polarity and breathing acquisition on image quality and intravoxel incoherent motion parameters—a pilot study. Radiology 2013;266(3):920–929.

158. Yoon JH, Lee JM, Yu MH, Kiefer B, Han JK, Choi BI. Evaluation of hepatic focal lesions using diffusion-weighted MR imaging: comparison of apparent diffusion coefficient and intravoxel incoherent motion-derived parameters. J Magn Reson Imaging 2014;39(2):276–285.

159. Kim YK, Lee MW, Lee WJ, et al. Diagnostic accuracy and sensitivity of diffusion-weighted and of gadoxetic acid-enhanced 3-T MR imaging alone or in combination in the detection of small liver metastasis (≤ 1.5 cm in diameter). Invest Radiol 2012;47(3):159–166.

160. Chung WS, Kim MJ, Chung YE, et al. Comparison of gadoxetic acid-enhanced dynamic imaging and diffusion-weighted imaging for the preoperative evaluation of colorectal liver metastases. J Magn Reson Imaging 2011;34(2):345–353.

161. Holzapfel K, Eiber MJ, Fingerle AA, Bruegel M, Rummeny EJ, Gaa J. Detection, classification, and characterization of focal liver lesions: value of diffusion-weighted MR imaging, gadoxetic acid-enhanced MR imaging and the combination of both methods. Abdom Imaging 2012;37(1):74–82.

162. Koh DM, Collins DJ, Wallace T, Chau I, Riddell AM. Combining diffusion-weighted MRI with Gd-EOB-DTPA-enhanced MRI improves the detection of colorectal liver metastases. Br J Radiol 2012;85(1015):980–989.

163. Taouli B, Vilgrain V, Dumont E, Daire JL, Fan B, Menu Y. Evaluation of liver diffusion isotropy and characterization of focal hepatic lesions with two single-shot echo-planar MR imaging sequences: prospective study in 66 patients. Radiology 2003;226(1):71–78.

164. Koh DM, Scurr E, Collins DJ, et al. Colorectal hepatic metastases: quantitative measurements using single-shot echo-planar diffusion-weighted MR imaging. Eur Radiol 2006;16(9):1898–1905.

165. Joo I, Lee JM, Yoon JH, Jang JJ, Han JK, Choi BI. Nonalcoholic fatty liver disease: intravoxel incoherent motion diffusion-weighted MR imaging-an experimental study in a rabbit model. Radiology 2014;270(1):131–140.

166. Van Beers BE. Science to Practice: can we diagnose nonalcoholic steatohepatitis with intravoxel incoherent motion diffusion-weighted MR imaging? Radiology 2014;270(1):1–2.

167. Rapacchi S, Wen H, Viallon M, et al. Low b-value diffusion-weighted cardiac magnetic resonance imaging: initial results in humans using an optimal time-window imaging approach. Invest Radiol 2011;46(12):751–758.

168. Delattre BM, Viallon M, Wei H, et al. In vivo cardiac diffusion-weighted magnetic resonance imaging: quantification of normal perfusion and diffusion coefficients with intravoxel incoherent motion imaging. Invest Radiol 2012;47(11):662–670.

169. Baur A, Stäbler A, Brüning R, et al. Diffusion-weighted MR imaging of bone marrow: differentiation of benign versus pathologic compression fractures. Radiology 1998;207(2):349–356.

170. Herneth AM, Philipp MO, Naude J, et al. Vertebral metastases: assessment with apparent diffusion coefficient. Radiology 2002;225(3):889–894.

171. Padhani AR, Makris A, Gall P, Collins DJ, Tunariu N, de Bono JS. Therapy monitoring of skeletal metastases with whole-body diffusion MRI. J Magn Reson Imaging 2014;39(5):1049–1078.

172. Ichikawa S, Motosugi U, Ichikawa T, Sano K, Morisaka H, Araki T. Intravoxel incoherent motion imaging of the kidney: alterations in diffusion and perfusion in patients with renal dysfunction. Magn Reson Imaging 2013;31(3):414–417.

173. Chandarana H, Lee VS, Hecht E, Taouli B, Sigmund EE. Comparison of biexponential and monoexponential model of diffusion weighted imaging in evaluation of renal lesions: preliminary experience. Invest Radiol 2011;46(5):285–291.

174. Gaing B, Sigmund EE, Huang WC, et al. Subtype differentiation of renal tumors using voxel-based histogram analysis of intravoxel incoherent motion parameters. Invest Radiol 2015;50(3):144–152.

175. Zhang JL, Sigmund EE, Rusinek H, et al. Optimization of b-value sampling for diffusion-weighted imaging of the kidney. Magn Reson Med 2012;67(1):89–97.

176. Lemke A, Stieltjes B, Schad LR, Laun FB. Toward an optimal distribution of b values for intravoxel incoherent motion imaging. Magn Reson Imaging 2011;29(6):766–776.

177. Leporq B, Saint-Jalmes H, Rabrait C, et al. Optimization of intra-voxel incoherent motion imaging at 3.0 Tesla for fast liver examination. J Magn Reson Imaging 2015; 41(5):1209–1217.

178. Cohen AD, Schieke MC, Hohenwalter MD, Schmainda KM. The effect of low b-values on the intravoxel incoherent motion derived pseudodiffusion parameter in liver. Magn Reson Med 2014;73(1):306–311.

179. Jambor I, Merisaari H, Aronen HJ, et al. Optimization of b-value distribution for biexponential diffusion-weighted MR imaging of normal prostate. J Magn Reson Imaging 2014;39(5):1213–1222.

180. Cho GY, Moy L, Zhang JL, et al. Comparison of fitting methods and b-value sampling strategies for intravoxel incoherent motion in breast cancer. Magn Reson Med 2014 Oct 9. [Epub ahead of print]

181. Iima M, Yamamoto A, Le Bihan D, et al. Computer-aided diagnosis of head and neck lesions from non-Gaussian diffusion MRI signal patterns [abstr]. In: Proceedings of the Twenty-Third Meeting of the International Society for Magnetic Resonance in Medicine. Berkeley, Calif: International Society for Magnetic Resonance in Medicine, 2015: 0687.